nature materials

ARTICLES

https://doi.org/10.1038/s41563-021-00993-6

Check for updates

Fast crystal growth at ultra-low temperatures

Qiong Gao[1,9], Jingdong Ai[2,9], Shixiang Tang[1], Minhuan Li[1], Yanshuang Chen[1], Jiping Huang[1], Hua Tong[3,4,5], Lei Xu[6], Limei Xu[2,7]✉, Hajime Tanaka[3,8]✉ and Peng Tan[1]✉

It is believed that the slow liquid diffusion and geometric frustration brought by a rapid, deep quench inhibit fast crystallization and promote vitrification. Here we report fast crystal growth in charged colloidal systems under deep supercooling, where liquid diffusion is extremely low. By combining experiments and simulations, we show that this process occurs via wall-induced barrierless ordering consisting of two coupled steps: the step-like advancement of the rough interface that disintegrates frustration, followed by defect repairing inside the newly formed solid phase. The former is a diffusionless collective process, whereas the latter controls crystal quality. We further show that the intrinsic mechanical instability of a disordered glassy state subject to the crystal growth front allows for domino-like fast crystal growth even at ultra-low temperatures. These findings contribute to a deeper understanding of fast crystal growth and may be useful for applications related to vitrification prevention and crystal-quality control.

Fast crystal growth from a deeply supercooled liquid[1–8] is a dynamic process of fundamental importance in condensed matter physics and material sciences[9,10]. In many industrial applications, it is crucial to prevent vitrification and increase the quality of crystals to be formed or to prevent crystallization of glasses. Classical theories of crystallization tell us that the crystal growth rate is given by $K(T)(1-\exp(-\Delta\mu/k_BT))$, where $K(T)$ is the kinetic factor expressing the rate of atom addition to the crystal, T is temperature, k_B is the Boltzmann constant and $(1-\exp(-\Delta\mu/k_BT))$ represents the thermodynamic factor, with $\Delta\mu=\mu_{liq}-\mu_{cry}$ being the chemical potential difference between liquid and crystal. In a deeply supercooled liquid, the thermodynamic factor approaches close to 1, whereas the kinetic factor, $K(T)$, crucially depends on the ordering kinetics, which has been a matter of intensive study[2,8–13].

The Wilson–Frenkel model considers diffusive ordering kinetics and predicts that $K(T)$ is governed by the translational diffusion constant $D(T)$ of the supercooled liquid[14,15]. In a deeply supercooled liquid, the structural relaxation time τ_α dramatically increases, and particle motions become subdiffusive. Thus, the crystal growth speed controlled by the diffusive transport is expected to drastically slow down towards the glass transition point T_g (refs. [4,6,8]). Unlike these models that assume diffusive transport, the collision-controlled model considers diffusionless ordering kinetics controlled by the thermal velocity and predicts that $K(T)\propto\sqrt{k_BT/m}$ where m is the particle mass[16], a relation that was shown to be responsible for the fast crystal growth[8].

Concerning the microscopic ordering kinetics in a shallowly supercooled liquid, recent studies reported that liquid structures with relatively large bond orientational order (BOO), 'precursor structures', always wet crystal surfaces[17–20]. Thus, a small adjustment is enough for the interface to transform to the crystal[18]. Furthermore, a flat or crystalline wall was shown to enhance not only crystal-like BOO but also layering (one-dimensional (1D) translational order) in the liquid–crystal interface[21], which may be viewed as a kind of wetting[22,23]. On the other hand, icosahedron-like structures formed due to the rapid supercooling frustrate crystallization[24]. A recent simulation work revealed that when the geometric frustration effect is negligible, fast crystal growth is due to the barrierless ordering of interface particles and characterized by constant $K(T)$ (ref. [25]). Colloidal experiments further observed crystal growth through a 'barrier-free jump' corresponding to the random walk of particles, which translates to collision-limited growth in atomic systems[26].

The dramatic slowing down of liquid diffusion upon cooling seems to suggest a barrierless ordering as the possible mechanism of fast crystal growth at deep supercooling[1,2,11,12,27,28]. However, this assumption is still waiting for experimental elucidation[21,25,29,30]. Moreover, rapid, deep supercooling tends to bring more disorder into the solid phase[9,31–34]. Thus, how the crystal growth process dissolves the disorder and determines the quality of the crystal is another critical problem.

To address these fundamental issues, we combine colloidal experiments with single-particle resolution[19,26,35–40] and numerical simulations and show that the fast crystal growth proceeds via barrierless collective motion at the interface without involving out-of-cage diffusion. Since fast crystal growth in the high-T regime has been well explained[25,26,41,42], we mainly focus on the low-T regime ($T\leq0.6T_m$, where T_m is the melting temperature; Methods, for the definition of the effective temperature).

We study the wall-induced fast crystal growth of a charged colloidal suspension (volume fraction $\phi\sim20\%$), in which colloids (diameter $\sigma\sim2.2\,\mu m$; polydispersity $\sim2\%$) interact via the screened Yukawa potential: $u(r)=\alpha\exp(-\kappa\sigma(r/\sigma-1))/(r/\sigma)$ for $r>\sigma$, with r being the distance from the centre, $1/\kappa$ being the Debye screening length in the suspension and α being the interaction strength parameter (the phase diagram on the $\kappa\sigma$–ϕ plane in Fig. 1a)[19,36,43]. To show the generality of the results to atomic/molecular systems, we also perform molecular dynamics simulations of particles interacting via the same potential. The details of the experiments and simulations are described in the Methods.

[1]State Key Laboratory of Surface Physics and Department of Physics, Fudan University, Shanghai, China. [2]International Centre for Quantum Materials and School of Physics, Peking University, Beijing, China. [3]Department of Fundamental Engineering, Institute of Industrial Science, University of Tokyo, Tokyo, Japan. [4]School of Physics and Astronomy, Shanghai Jiao Tong University, Shanghai, China. [5]Department of Physics, University of Science and Technology of China, Hefei, China. [6]Department of Physics, The Chinese University of Hong Kong, Hong Kong, China. [7]Collaborative Innovation Center of Quantum Matter, Beijing, China. [8]Research Center for Advanced Science and Technology, University of Tokyo, Tokyo, Japan. [9]These authors contributed equally: Qiong Gao, Jingdong Ai. ✉e-mail: limei.xu@pku.edu.cn; tanaka@iis.u-tokyo.ac.jp; tanpeng@fudan.edu.cn

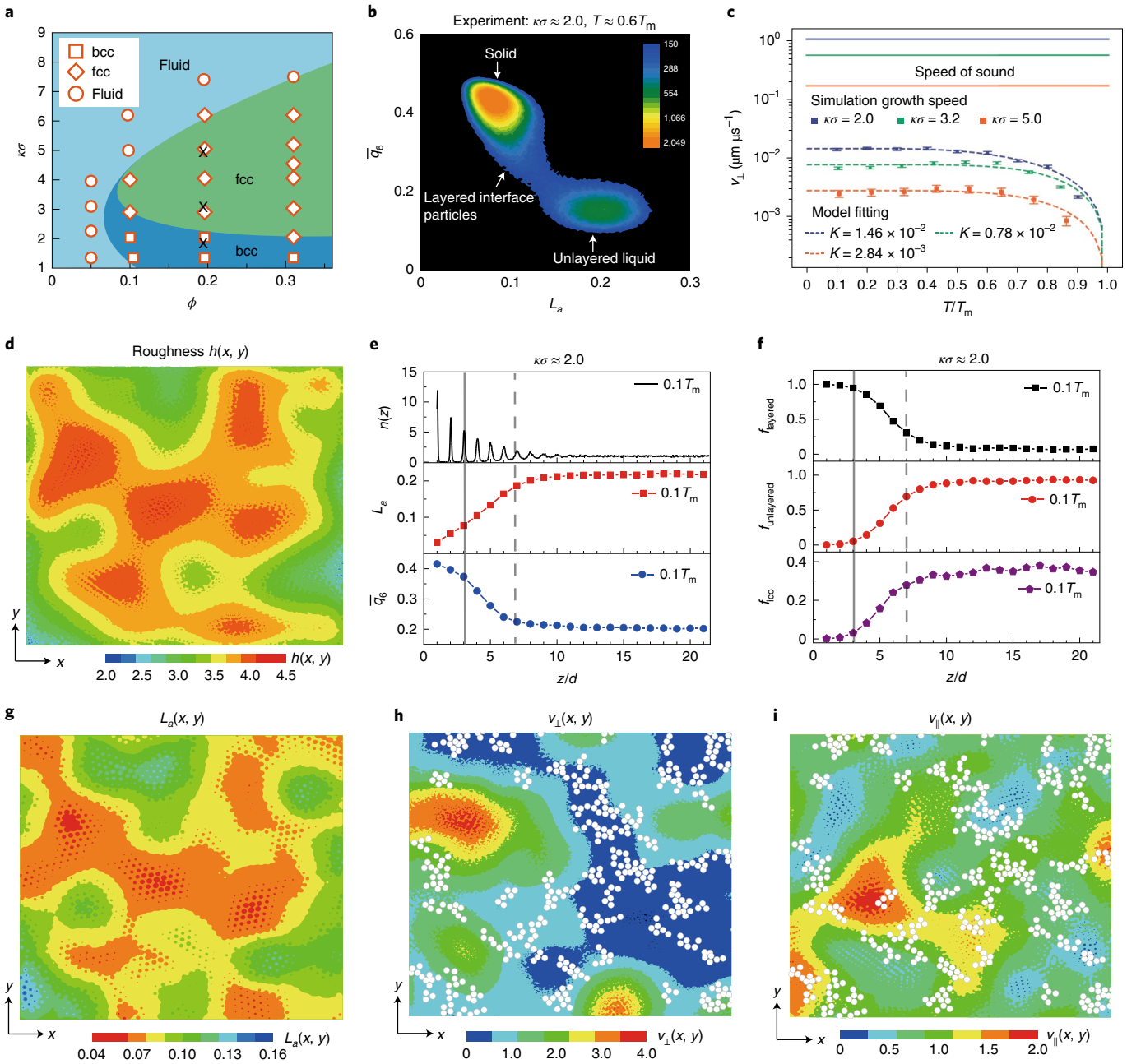

Fig. 1 | The interface profile of fast crystal growth. a, Phase diagram on the $\kappa\sigma$–ϕ plane of our charged colloidal system measured in the experiments. Data points verified by simulations are specified by a black X. **b**, Particle counts (on a logarithmic scale) on the $L_a - \bar{q}_6$ plane during crystal growth. The left group with $L_a < 0.14$ is composed of layered particles, and the right group is composed of unlayered particles. The layered particles in the left group with $\bar{q}_6 < \bar{q}_6^*$ (~ 0.35) are defined as 'layered interface particles'. **c**, Crystal growth speed $v_\perp$ determined by simulations. The error bars represent the standard deviation of the growth speed measurements. It can be fitted with a temperature-independent constant kinetic factor, $K(T)$. The fast crystal growth can be observed at a temperature as low as $0.1T_m$, which is much lower than the spinodal crystallization temperature $T_{sp} \approx 0.7T_m$. The speed of sound is shown by a solid horizontal line for each sample. **d**, The rough interface illustrated by the contour plot of the height of the crystal front $h(x, y)$ in the z direction ($\kappa\sigma \approx 2.0$, $T \approx 0.1T_m$ in simulation). **e**, Interface profile illustrated by the particle number density $n(z)$ (top), $L_a(z)$ (middle) and $\bar{q}_6(z)$ (bottom) with respect to z/d. The interface roughness h is defined as the distance over which $\bar{q}_6(z)$ changes from 75% (grey solid line, defined as $\bar{q}_6^*$) to 10% (grey dashed line) of its value in the final crystal relative to its value in the unlayered liquid. **f**, Interface profile illustrated by the fraction of layered structures $f_{layered}$ (top), unlayered structures $f_{unlayered}$ (middle), and icosahedron-like structures f_{ico} (bottom) in each layer. The rough and thick interface provides a large contact area that disintegrates the abundant icosahedron-like structures (~30% in the unlayered liquid). **g**, Contour plot of the layering parameter $L_a(x, y)$ for the particle layer closest to the grey solid line in panels **e** and **f**. We can see its good correspondence with $h(x, y)$ in panel **d**. **h**,**i**, Contour plots of the vertical growth speed $v_\perp(x, y)$ (**h**) and the lateral growth speed $v_\parallel(x, y)$ (**i**) calculated after a time $\Delta t \approx 500\,\mu s$. The icosahedron-like structures at the initial interface area (in between the grey solid and dashed lines in panels **e** and **f**) are represented by the white spheres. We can see that the icosahedron-like structure is mainly eliminated by the lateral growth.

We use the bond orientational order parameters (q_l and w_l) and their coarse-graining versions ($\overline{q}_l$ and $\overline{w}_l$, respectively) to quantify the single-particle-level local structures (details in Methods). We employ a T-dependent threshold $\overline{q}_6^\star$ to distinguish solid from liquid (definition in Methods).

Interface structure profile during fast crystal growth. Many studies revealed the preordering of liquid structures at the liquid–crystal interface, which is characterized by the layering of particle positions and the relatively large BOO $\overline{q}_6$ (refs. [17–20,23,36,44,45]). However, such preordering itself does not guarantee fast crystal growth at deep supercooling, because the advancement of the preordered region might suffer from slow liquid diffusion and geometric frustration at deep supercooling.

To provide the microscopic information of preordering, we design a single-particle-level layering parameter $L_a(i)$, which quantifies the 1D positional fluctuation of particle i along the growth direction (perpendicular to the smooth capillary wall). $L_a(i)$ can be regarded as the 1D version of the Lindemann parameter. Typically, $L_a \approx 0.22$ for disordered particles, whereas $L_a < 0.14$ for crystalline particles (Methods and Extended Data Fig. 1a).

By using the counting plots on the $L_a - \overline{q}_6$ plane, we illustrate structural ordering during crystal growth in Fig. 1b (at $\kappa\sigma \approx 2.0$, $T \approx 0.6T_m$ in the experiment). Besides the solid ($\overline{q}_6 \geq 0.35$; here $\overline{q}_6^\star(0.6T_m) \approx 0.35$), we observe a bridging region ($\overline{q}_6 < 0.35$, $L_a < 0.14$) between the solid (the upper-left island in Fig. 1b) and the unlayered liquid (the lower-right island in Fig. 1b). This bridging region comes from layered interface particles ($\overline{q}_6 < 0.35$, $L_a < 0.14$) consisting of both the solid surface (connected to the solid) and layered interface liquid (Extended Data Fig. 1b,c). This bridging in the order-parameter space implies that preordering is a consequence of the non-trivial coupling between the preexisting crystals and structural fluctuations (bond orientational and positional) in the supercooled liquid. We confirm that this feature is always observed in the entire crystallization process in both experiments and simulations (Extended Data Fig. 2).

Surprisingly, we find that the crystal growth speed obtained from our simulations (before spinodal nucleation happens in the bulk liquid region of the sample; Extended Data Fig. 3) can be almost fitted by a T-independent kinetic factor $K(T)$. This speed is about two orders of magnitude slower than the longitudinal sound speed, the theoretical upper limit of the growth velocity[16,46], as shown in Fig. 1c for three typical values of $\kappa\sigma$ (indicated by X in Fig. 1a). The fast crystal growth can take place at a temperature as low as $0.1T_m$, allowing us to uncover its microscopic ordering kinetics.

We show the microscopic processes of the fast crystal growth at $0.1T_m$ for typical samples ($\kappa\sigma \approx 2.0$, simulation) in Fig. 1d–i. A critical feature is that the solid–liquid interface is rough and thick. We can see this in the contour plot of the height of the crystalline islands close to the vicinity of the growth front, $h(x,y)$, in Fig. 1d, and the gradual change of the order parameters—$n(z)$ (particle number density, top panel), $L_a(z)$ (middle panel) and $\overline{q}_6(z)$ (bottom panel)—as a function of z/d (with d being the average layer–layer distance along the z direction) in Fig. 1e. We define the interface roughness h as the crystalline islands' average height, and the interface thickness l as the width of the preordered layers that cover the crystalline islands (Methods). We find that the rough and thick interface ($h \approx 4.6d$ and $l \approx 3.5d$ at $\kappa\sigma \approx 2.0$) is a general characteristic observed at all T for both experiment and simulations (Extended Data Fig. 4 and Supplementary Figs. 1 and 2). The rough and thick interface surrounds disordered liquid regions with many icosahedron-like structures (~30%). Although icosahedral structures are known to impede crystallization in bulk, the large contact area between the preordered interface and the liquid surrounded by it effectively disintegrates the icosahedron-like structures, as shown in Fig. 1f (also Extended Data Fig. 4c).

We briefly consider the nature of the preordering, layering and crystal-like BOO, at the rough crystal-growth front. In single-component liquids with isotropic interactions, three-dimensional (3D) crystal-like BOO generally develops in a supercooled state but without any translational order before crystals form[27,30]. The unique feature of the above ordering is that besides 3D crystal-like BOO, the interface possesses 1D translational order due to the coherent phase selection of the density wave by the crystal surface or the wall[21]. We note that the layering thickness, controlled by the positional correlation length ξ_T, is rather T insensitive. On the other hand, the correlation length of crystal-like BOO, ξ_{BOO}, grows for deeper undercooling for a flat wall but is constrained by ξ_T for a curved wall[21]. This is consistent with the relation of $h \approx l \approx \xi_T$ for all T (Fig. 1e and Extended Data Fig. 4).

Owing to the rough, thick nature of the interface, we find an elementary island-growth process composed of the crystal's vertical and lateral growth that reflects the competition between wall-induced preordering at the crystal growth front and disordering due to icosahedrons in the bulk liquid (Fig. 1g–i). Fast vertical growth happens mainly at the locations where the layering effect wins over the geometric frustration effect of the icosahedrons (compare the contour plot of the layer parameter $L_a(x,y)$ (Fig. 1g; the particle layer closest to the grey line in Fig. 1e) and the vertical growth speed $v_\perp(x,y)$ (Fig. 1h, calculated after a time period $\Delta t \approx 500\,\mu s$; white spheres represent icosahedron-like structures in between the grey and dashed lines in Fig. 1f). The lateral growth process mostly eliminates the icosahedron-like structures (the contour plot of the lateral growth speed $v_\perp(x,y)$ in Fig. 1i), which generally happens around the crystal islands (compare Fig. 1d,g,i). The island-growth modes are robustly observed at both deeply quenched ($T \leq 0.6T_m$, with abundant icosahedron-like structures) and shallowly quenched ($T \geq 0.7T_m$, with sparse icosahedron-like structures) samples (Extended Data Fig. 5 and Supplementary Fig. 3). This observation again suggests that the rough and thick preordered interface is a critical feature that allows fast crystal growth.

Interestingly, although the growth process is spatially inhomogeneous, the moving distance of the growth front during the ordering time Δt typical of one particle layer (Extended Data Fig. 6) is approximately equal to the interface thickness l, suggesting a collective nature of the ordering. We will consider the physical conditions required for low-T collective ordering later.

Microscopic kinetic pathways of low-T fast crystal growth. Here we consider how the interface gains order and transforms to the crystal at deep supercooling. As implied by the structural ordering pathway in Fig. 1b (also Extended Data Fig. 7), we find that the crystallization proceeds via two processes, as schematically shown in Fig. 2a: the two-step propagation of the crystal growth front and the slow removal of defective structures in the newly formed crystal. The increase in the crystalline particle N_{solid} with time t is shown in Fig. 2b for an experiment and Fig. 2d for a simulation. The essential characteristics are common to both. From $t1$ to $t2$, the rapid crystal growth occurs, as seen in Fig. 2b,d. This process leads to the formation of fresh solid ($\overline{q}_6$ slightly exceeds $\overline{q}_6^\star$), characterized by an increase of $\overline{q}_6$ that crosses $\overline{q}_6^\star$ in Fig. 1b. At $t2$, this newly formed fresh solid ($\overline{q}_6 \approx \overline{q}_6^\star$) is covered by the poorly ordered interface ($L_a \approx 0.14$, formed from $t1$ to $t2$). This new unmoving interface gradually gains order in the period from $t2$ to $t3$, characterized by the change of L_a and $\overline{q}_6$ from the left side of the unlayered liquid island, $L_a \approx 0.14$, to the bottom side of the solid islands in Fig. 1b, that is, to a value of $\overline{q}_6$ comparable to the interface at $t1$. Defect removal in the newly formed crystal also proceeds from $t2$ to $t3$, which increases the crystal quality and promotes the new interface's preordering (Fig. 2c,e). At $t3$, the new interface becomes preordered enough to initiate the rapid crystal growth again over the distance of ξ_T. This step-like growth process means that the advancement of

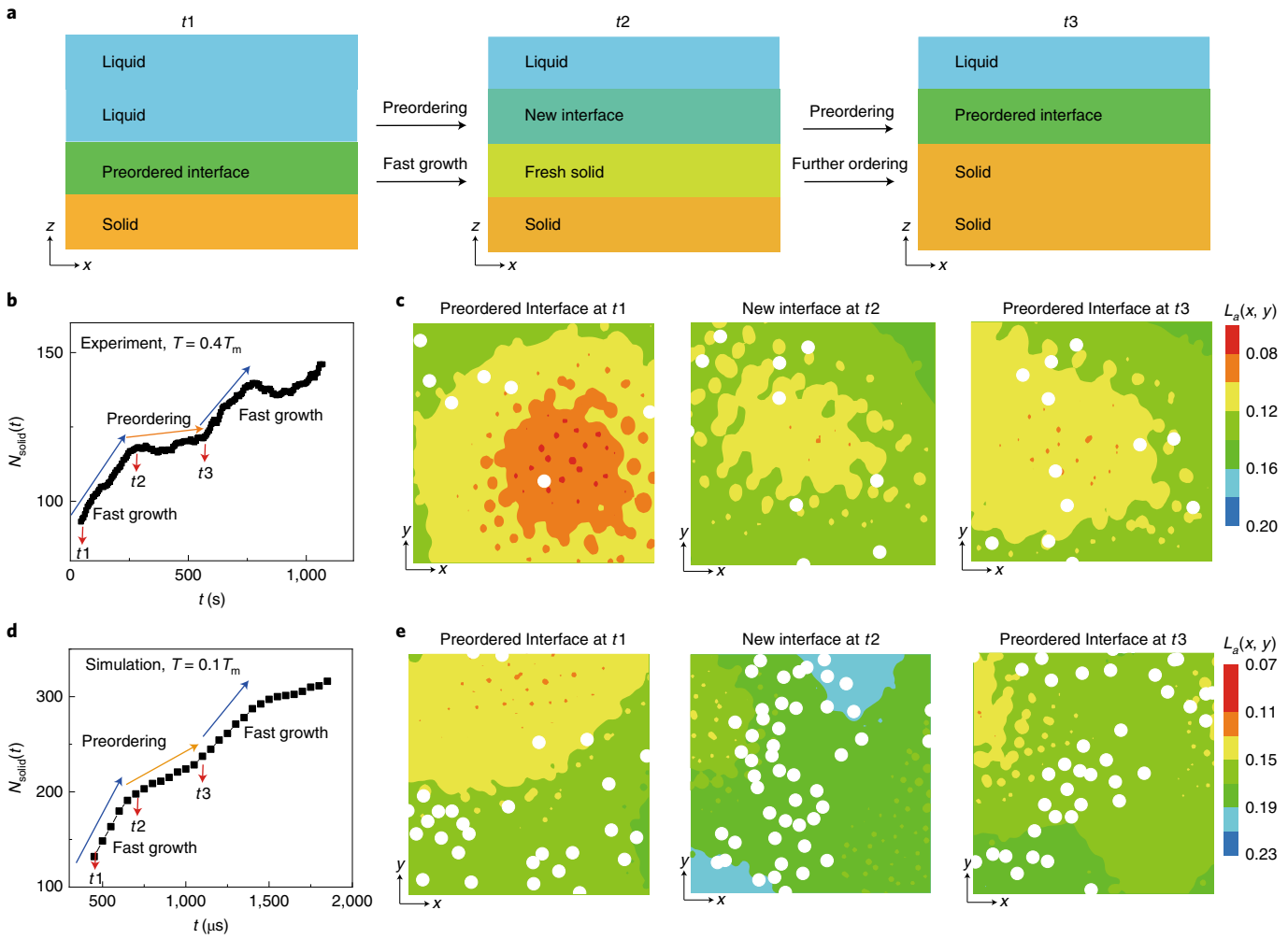

Fig. 2 | Step-like advancement of crystal growth front. a, Schematic figures explaining the fast crystal growth process. For the meanings of *t*1, *t*2 and *t*3, see the following panels. **b**, Solid particle number N_{solid} as a function of *t* in the small field of view (panel **b**) in experiments ($\kappa\sigma = 3.2$, $T = 0.4T_m$). Note that the curve is smoothed in order to reduce the particle number fluctuation. We can see the presence of two distinct repetitive steps. **c**, The layer parameter $L_a(x, y)$ of the interface layers at *t*1 (left), *t*2 (middle) and *t*3 (right). We can see the decrease of L_a from *t*2 to *t*3, which means the increase of the degree of layering (that is, preorder) in the interface, and then the initiation of another round of fast growth. Icosahedron-like structures at the interface are represented by white spheres. **d**,**e**, The same quantities as in panels **b** and **c** for simulations ($\kappa\sigma = 2.0$, $T = 0.1T_m$). The behaviours are similar to the experimental ones. Here we note that as the size of the field of view increases, the two-stage feature is gradually lost, reflecting a spatial inconsistency in the phase of crystal growth.

the interface requires a certain crystal-quality level of the underlying crystal.

Now we focus on the physical mechanism of this peculiar fast crystal growth. First, we define the time required for this process as ordering time (τ), and the distance over which a particle moves during the process as moving distance (r). To keep the consistency, here we use the same value of $\bar{q}_6^*(T)$ to calculate the interface thickness $l(T)$ and the ordering time $\tau(T)$ at each temperature T. Interestingly, we observe a nearly T-independent probability distribution $p(\tau)$ at $\kappa\sigma \approx 2.0$, as shown in Fig. 3a (simulations; Supplementary Fig. 4 for other $\kappa\sigma$). The average ordering time τ_{ave} is several times longer than the time τ_E (~56 μs) corresponding to the Einstein frequency of an equilibrium crystal at $0.5T_m$, whereas the moving distance r in Fig. 3b is much shorter than the lattice constant a. On noting that both the long-time diffusive particle motion and the ballistic particle motion are sensitive to T, the T-insensitive τ_{ave} and small r point to the 'barrierless' ordering kinetics associated with the cooperative motion of interface particles without involving 'out-of-cage' diffusion.

To elucidate the transformation kinetics in more detail, we show in Fig. 3c the time-dependent mean-square displacement $\langle \Delta r(t)^2 \rangle$ of equilibrium crystals, together with the two timescales, τ_E (~56 μs) and τ_{ave} (that is, the average of τ; the vertical light blue and green lines, respectively). We can see that τ_E is comparable to when $\langle \Delta r(t)^2 \rangle$ first reaches its plateau, that is, the interparticle collision time. During τ_{ave}, several times longer than τ_E, $\langle \Delta r(t)^2 \rangle$ oscillates around the plateau, implying that the collisions are frequent enough to induce a collective motion of particles in the interface. The collective nature of the liquid-to-crystal transformation can also be seen in the displacement field Δr of two particle layers formed during τ_{ave} (Fig. 3d (simulations) and Fig. 3e (experiments)): the moving distance shorter than a and the spatially extended correlation of displacement vectors over a few particle distances indicate that the collective particle motion mainly drives the barrierless ordering, that is, 'diffusionless ordering'.

Such diffusionless ordering suggests the following expression of the crystal growth speed: $v(T) \approx l(T)/\tau_{ave}(T)$, where $l(T)$ is the interface thickness. We use this relation to predict the crystal growth speed for $T \leq 0.6T_m$, where we observe a similar growth mode as in Fig. 1d–i, and find that the predicted value agrees quite well with the growth speeds obtained by simulations and experiments for various

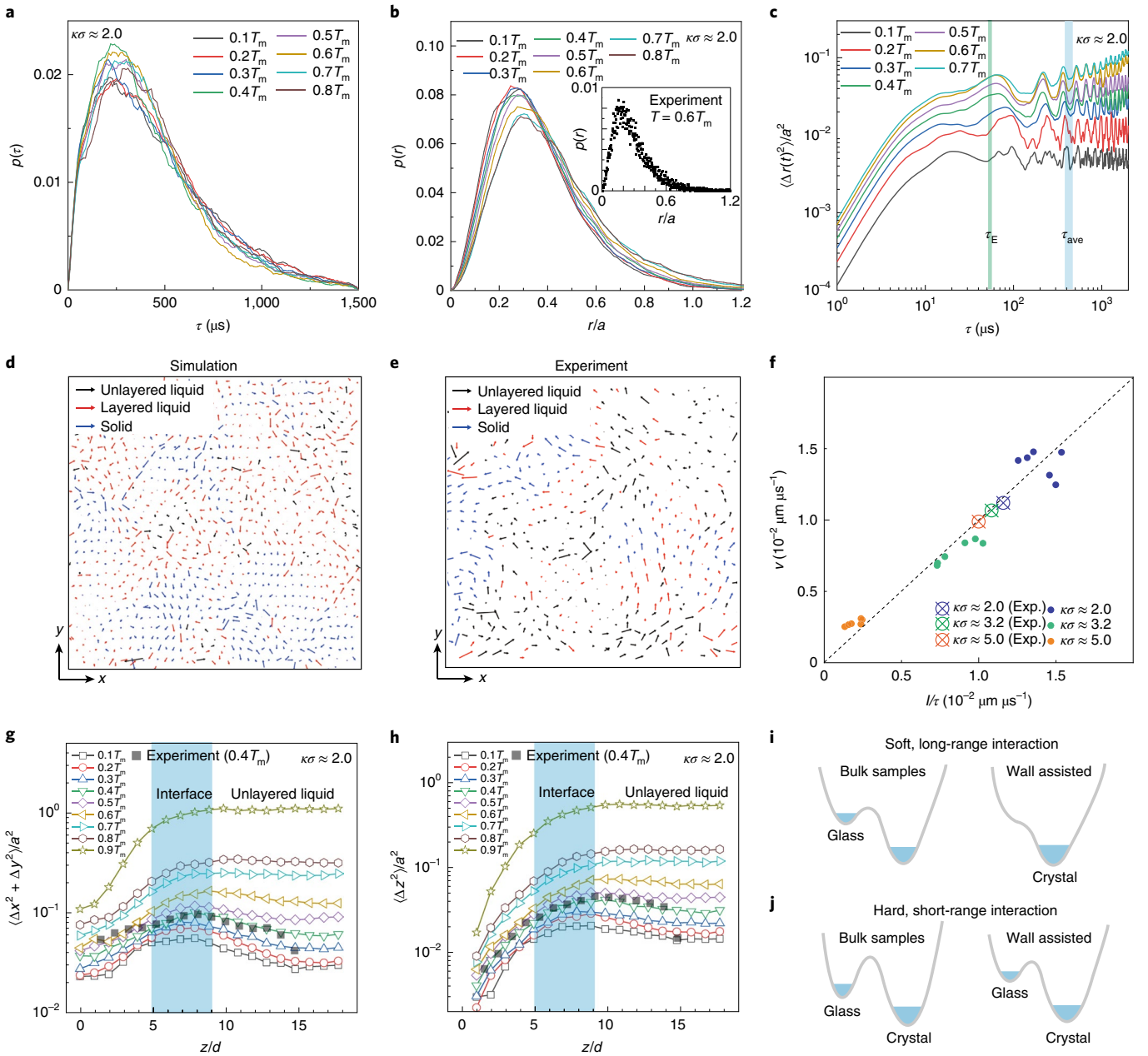

Fig. 3 | The crystal growth speed determined by the barrierless ordering. a, Probability distribution $p(\tau)$ of particles spending time τ passing through the preordered state at various T ($\kappa\sigma \approx 2.0$ in simulations). We observe the T-independent distributions. **b**, Probability distribution $p(r)$ of particles' moving distance r (corresponding to **a**) in the unit of the lattice constant a. Inset, the result of an experiment at $T \approx 0.6T_m$. The moving distance r is much shorter than a. **c**, The time-dependent mean-square displacement $\langle \Delta r(t) \rangle$ of equilibrium crystals at various T values. We indicate two timescales corresponding to the Einstein frequency ($\tau_E \approx 56$ μs) and τ_{ave} by the vertical green and light blue lines, respectively. **d**,**e**, The displacement fields for two particle layers in the x–y plane during a time interval of τ_{ave} in simulations (**d**) and experiments (**e**). The arrow colours represent the structure types. We can see cooperative, small particle motions. **f**, Agreement between the prediction of the diffusionless growth model and measurements for the crystal growth speed v. We determine v as $v \approx l/\tau_{ave}$ in the model, where l is the interface thickness. Exp., experimental. **g**,**h**, The z/d dependence of the mean-square displacement $\langle \Delta x(\tau_{ave})^2 + \Delta y(\tau_{ave})^2 \rangle$ in the x–y plane (**g**) and $\langle \Delta z(\tau_{ave})^2 \rangle$ in the z direction (**h**) calculated in a time period of $1.5\tau_{ave}$. The particle motion at the interface (blue area) is enhanced at $T < 0.6T_m$, especially in **h**. **i**, The schematic illustration of the potential-energy landscape for a bulk sample and a sample with a flat wall for systems with soft, long-range interactions. The potential-energy landscape of the bulk sample has two basins (glass and crystal; left panel). However, in contact with a wall, the glass state becomes unstable subject to the crystal growth front (right panel). **j**, The schematic illustration of the potential-energy landscape for systems with hard, short-range interactions. In this case, the two local minima remain even with the presence of a wall.

$\kappa\sigma$ and T (Fig. 3f). These results indicate that the T insensitivity of $K(T)$ in our system should originate from the T insensitivities of l and τ_{ave} (Extended Data Fig. 8 on the effect of the selection of $\overline{q}_6^*$ on the result). Here we note that the growth speed in experiments is slower by a factor of 1.5×10^6 than that in molecular dynamics simulations due to viscous friction in the experiments.

The cooperative and barrierless ordering kinetics lead us to a conjecture that the supercooled or glass state is intrinsically

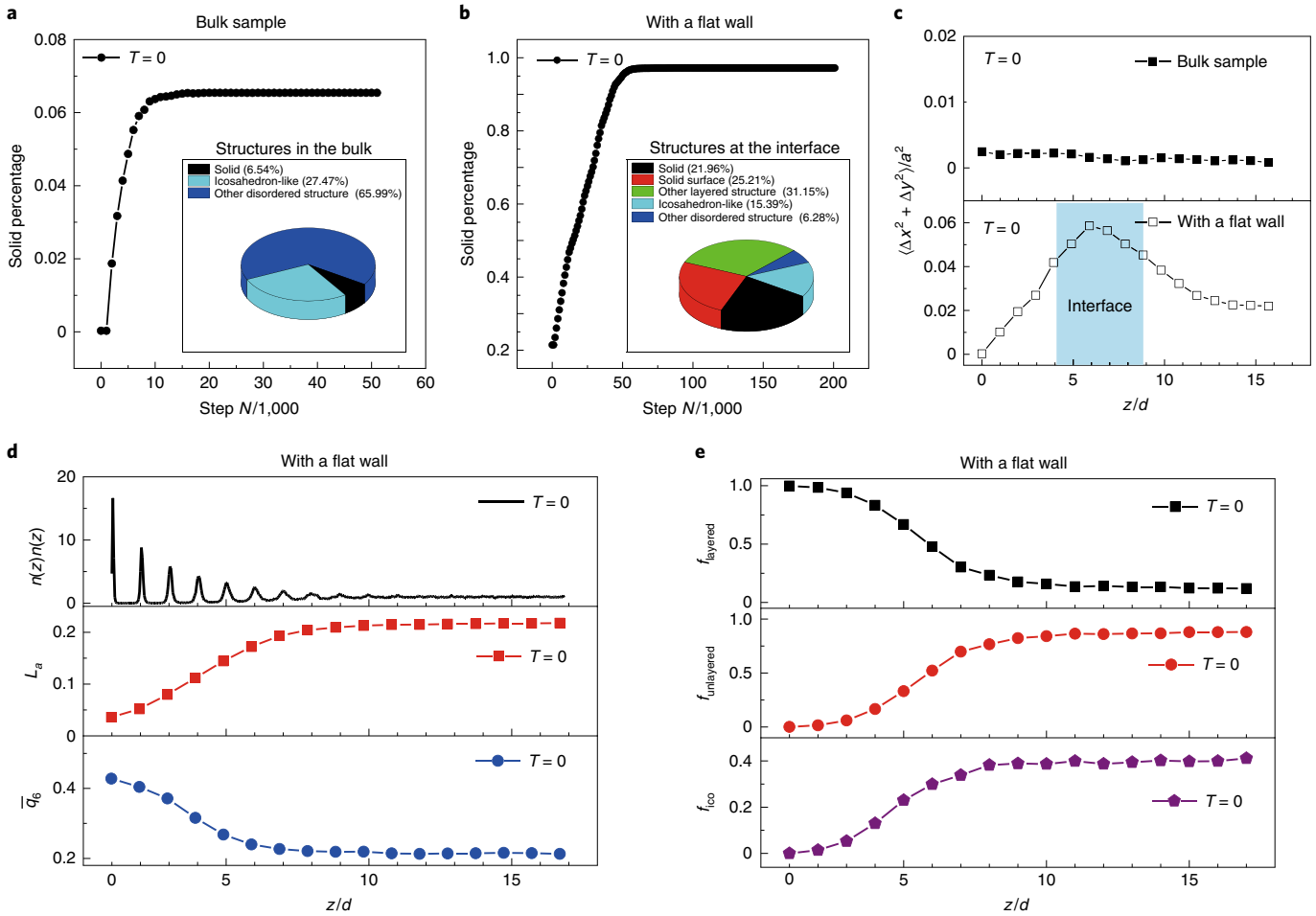

Fig. 4 | The crystal growth for $\kappa\sigma \approx 2.0$ at $T = 0$. a, Solid percentage versus the step N of energy minimization at $T = 0$ for bulk samples. A glass state is formed. The inset figure shows the final structure. **b**, Solid percentage versus the step N of energy minimization at $T = 0$ for samples with a flat wall. A crystal state is eventually formed by crystal growth. The inset figure shows the interface structure. **c**, The mean-square displacement ($\Delta N = 10 \times 10^3$, averaged in a period $1.5\Delta N$) for the sample in **a** and in **b**. We observe a similar particle-mobility enhancement at the interface (blue) as in low-T crystal growth (Fig. 3g). **d**, Interface profile in **b** illustrated by the particle number density $n(z)$ (top), $L_a(z)$ (middle) and $\bar{q}_6(z)$ (bottom) with respect to z/d. **e**, Interface profile illustrated by the fraction of layered structures f_{layered} (top), unlayered structures $f_{\text{unlayered}}$ (middle) and icosahedron-like structures f_{ico} (bottom) with respect to z/d. A similar rough and thick interface is observed as in low-T samples.

unstable, not only thermodynamically but also mechanically, when subjected to the crystal growth front. This conjecture is supported by the particle-mobility enhancement at the crystal growth front: we can see the characteristic peak in the z/d dependence of the mean-square displacement $\langle \Delta x(\tau_{\text{ave}})^2 + \Delta y(\tau_{\text{ave}})^2 \rangle$ in the x–y plane (calculated in a time period of $1.5\tau_{\text{ave}}$), as shown in Fig. 3g (simulations at $0.1T_{\text{m}} \leq T \leq 0.6T_{\text{m}}$ and an experiment at $T \approx 0.4T_{\text{m}}$). At $T > 0.6T_{\text{m}}$, the liquid diffusion is faster than the growth-front induction, and thus there is no mobility enhancement. In previous studies[41,42], a liquid-diffusion-limited model explains the upper-bound crystal growth speed for shallow quenches. We find that the crystal growth speeds predicted by the two models based on the diffusive and non-diffusive barrierless orderings cross around $T = 0.5T_{\text{m}}$ (comparison in Extended Data Fig. 9); only below $T = 0.5T_{\text{m}}$ is the mobility-enhancement effect around the interface pronounced. The intrinsic mechanical instability of the supercooled or glass state subject to the crystal growth front at deep supercooling can solve the contradiction between slow liquid diffusion and fast crystal growth. The particle-mobility enhancement in the z direction is not as obvious as in the x–y plane (Fig. 3h), suggesting the primary role of the cooperative lateral particle motion.

We propose a schematic illustration of the potential-energy landscape for fast crystal growth (Fig. 3i,j). In our low-ϕ charged colloidal systems with soft, long-range interactions (Fig. 3i), there are two basins (glass and crystal) for bulk samples, whereas the supercooled or glass state subject to the crystal growth front is mechanically unstable for samples with a flat wall so that the crystallization proceeds via wall-induced barrierless ordering. By contrast, when the interaction becomes hard and short range, icosahedron-like structures are too hard to be disintegrated. Therefore, the supercooled or glass state cannot be unstable at low enough T, even in contact with the crystal. Thus, the glass–crystal conversion cannot be barrierless (that is, no crystal growth; Extended Data Fig. 10)[25,47]. This suggests that the potential-energy landscape still has two basins, even in the presence of a smooth wall (Fig. 3j). We also note that the mechanical stability of glasses is also affected by the crystal–liquid density difference (Supplementary Discussion and Supplementary Figs. 5–12).

To verify the above physical picture, we perform simulations that rapidly quench the equilibrium liquid at $T = 1.05T_{\text{m}}$ to $T = 0$, at which the thermal fluctuation is absent, and the potential-energy minimization is the only driving force of solidification (Methods). Bulk samples robustly form a mechanically stable glass state (Fig. 4a),

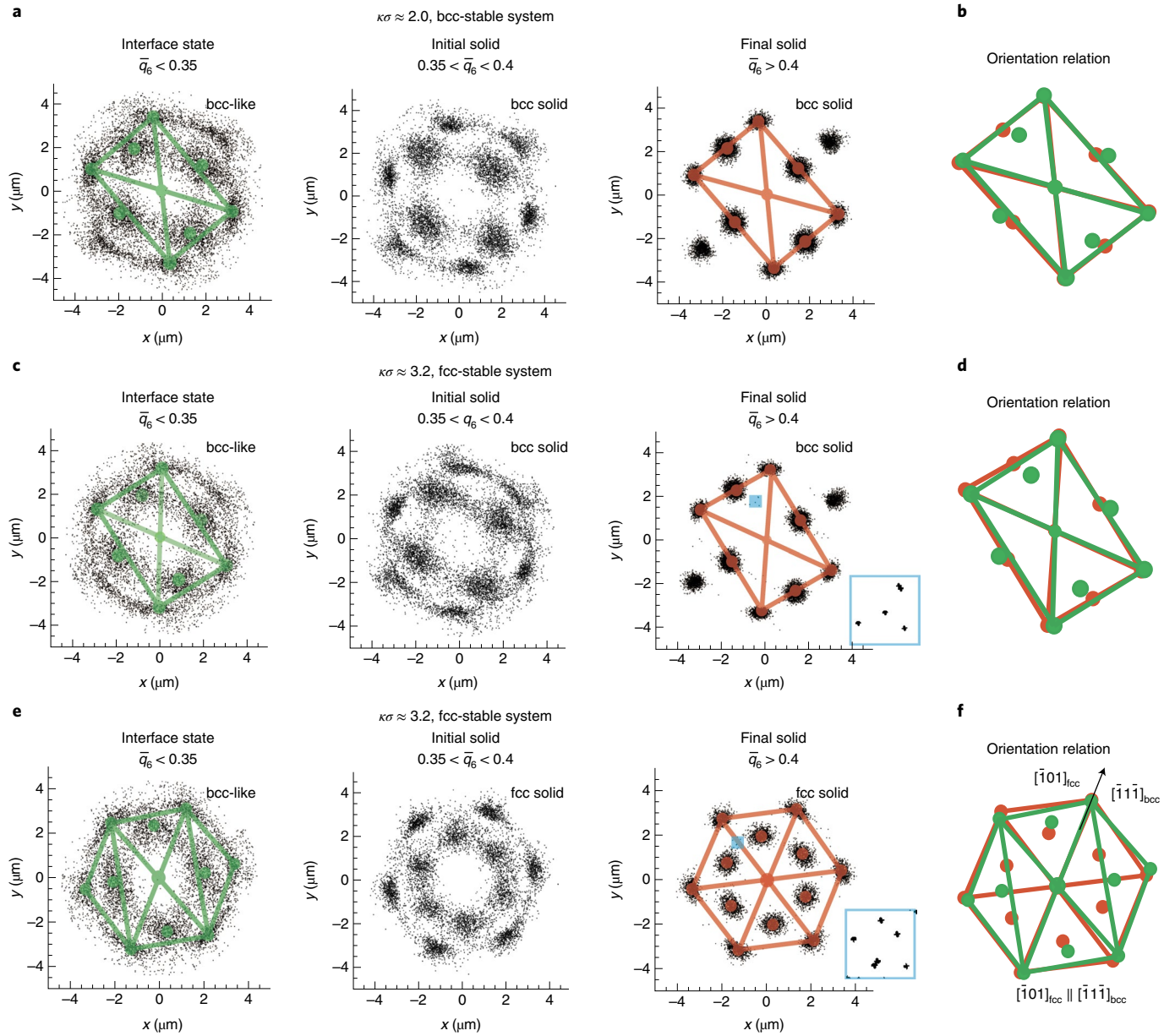

Fig. 5 | Orientational relations and the structure ordering inside the solid phase. a–f, The local-order development for a group of layered particles ($L_a < 0.14$) that grow to the same crystalline grain. We first shift each particle to a central reference point ($x = y = z = 0$), and then, indicate the relative positions of its neighbouring particles by the black dots. We classify the particles into three parts, based on their $\bar{q}_6(i)$: interface stage ($\bar{q}_6(i) < \bar{q}_6^{\star}$), initial solid ($\bar{q}_6^{\star} < \bar{q}_6(i) < 0.4$) and final solid ($\bar{q}_6(i) > 0.4$). The average is taken both in time and space. The average configuration can be identified through the most-probable fitting. In the bcc-stable system (**a** and **b**), we observe hidden bcc-type order at the interface stage (the left panel in **a**), and the quenched-in disorder is reduced through the further structure ordering (the middle and right panels in **a**). The bcc solid is formed via the solid-to-solid-like shuffle transformation, as shown in panel **b**. In the fcc-stable system (**c–f**), we also observe hidden bcc-type order at the interface stage, but it transforms to a fcc solid via two different pathways. We can clearly see the unreleased residual disorder that is trapped in the interstitial sites in the right panels of **c** and **e** (blue squares, enlarged in the insets). The transformation to a metastable bcc solid in panels **c** and **d** is the shuffle type as in panels **a** and **b**, whereas the transformation to a fcc solid in panels **e** and **f** is martensitic with the Kurdjumov–Sachs orientation relation ($(111)_{fcc} \parallel (110)_{bcc}$, $[\bar{1}01]_{fcc} \parallel [\bar{1}\bar{1}\bar{1}]_{bcc}$). In **a–f**, green and brown diagrams represent the structures in 'interface state' and 'final solid', respectively. The arrow in **f** represents the direction of $[\bar{1}01]_{fcc}$ and $[\bar{1}\bar{1}\bar{1}]_{bcc}$ axes.

as expected, suggesting that they have inherent amorphous structures. Surprisingly, the same sample with a flat wall shows crystal growth until full crystallization (Fig. 4b) while accompanying the distinct particle-mobility enhancement selectively around the interface (Fig. 4c). The interface profiles are also very similar to those at finite temperatures (Fig. 4d,e). These findings firmly verify the above scenario that the glass state subject to the crystal growth front is intrinsically unstable mechanically in systems with soft, long-range interactions. We emphasize that the absence of thermal excitation at $T = 0$ indicates the instability's purely mechanical nature, reminiscent of the domino-like mechanism.

Structural ordering inside the solid phase. Due to cooperative, fast layering, we find that each preordered layer does not have the same number of particles, introducing disorder to the newly formed crystal ($\bar{q}_6 \approx \bar{q}_6^{\star}$, ~0.35 at $0.6T_m$). In previous studies[31,32,34,48],

this phenomenon was interpreted as defect trapping or dynamic broadening of the solid–liquid interface. Thus, the newly formed crystal still needs further structural ordering to reduce the residual 'liquid-like' defective structures trapped inside the solid phase, necessary for the next round of ordering. This secondary process is critical for the quality control of crystals.

Structural transformations in solids generally require a specific orientational relationship between the parent and the product structures, as in solid-to-solid transitions[49]. By using the spherical projection method, which keeps the orientational information, we examine the possible orientational connections among each ordering stage and a group of interface particles ($L_a < 0.14$) that grow to the same crystalline grain (Methods). Interestingly, we find a body-centred cubic (bcc) type of orientational ordering hidden behind positional fluctuations at the interface stage (left panel of Fig. 5a for typical bcc-stable samples ($\kappa\sigma \approx 2.0$)). As the ordering proceeds, the quenched-in disorder, the source of point defects in solids, is reduced, and eventually, a bcc solid is formed (the middle and right panels of Fig. 5a). This ordering process can be understood as a solid-to-solid-like shuffle transformation requiring only minor adjustment of a few neighbouring particles, as shown by the orientation connection in Fig. 5b. A similar ordering process was also observed for homogeneous crystallization in bulk[18].

The local ordering process in the face-centred cubic (fcc), stable system ($\kappa\sigma \approx 3.2$) is more complicated than the above case. We also find the dominance of bcc-type ordering hidden behind fluctuations at the interface stage. Then, as liquid-like fluctuations decrease, both metastable bcc and stable fcc solids can be formed, as shown in Fig. 5c,e, respectively. We can clearly see the unreleased residual disorder trapped in the interstitial sites (the blue regions and insets of the right panels of Fig. 5c,e). The formation process of the bcc solid is again a shuffle transformation, as shown in Fig. 5d. Surprisingly, the formation of the fcc solid from the preordered interface is a martensitic transformation with the so-called Kurdjumov–Sachs orientation relation ($(111)_{fcc} \| (110)_{bcc}$, $[\bar{1}01]_{fcc} \| [\bar{1}\bar{1}\bar{1}]_{bcc}$), as shown in Fig. 5f. A similar Kurdjumov–Sachs orientation relation was also observed in simulations of homogeneous crystallization in bulk[50].

The barrierless ordering kinetics with specific orientational relations suggest that the crystal quality is controlled by a cooperative interplay between the liquid and solid orders[36]. The interplay constrains the liquid-like defective structures to a few limited configurations having specific orientational connections to the solid, which may be characteristic of the wetting of a liquid with internal order to the solid. Thus, the process of crystal-quality improvement takes structure transformation pathways determined by specific orientational connections.

Outlook

We have shown that fast crystal growth with a domino-like growth mode requires the ability to induce a rough and thick preordered interface that overcomes the geometric frustration and has the ability to accommodate and eradicate the trapped-in disorder (fluctuations of particle numbers in each layer). The presence of these two conditions provides a general explanation about why a specific crystalline plane satisfying the conditions could induce the fastest growth[51].

Another critical factor enabling ultra-low-temperature crystal growth is the intrinsic mechanical instability of the disordered state subject to the crystal growth front, which causes a domino-like crystal growth mode. To maintain this mode, the secondary ordering ability of the initially formed solids is crucial; otherwise, the growth process would become slower as the trapped-in disorder accumulates more and more. In our low-ϕ charged particle systems, the interaction is soft, and thus, the trapped-in disorder can easily transform to interstitials, which do not break the solid's translational order. By contrast, when the interaction becomes harder, the crystal–liquid density mismatch increases. With icosahedral structures' rigidity, this large density mismatch makes both the ordering at the interface and the secondary ordering of the crystal difficult. For a hard enough interaction, thus, the domino-like growth mode is not possible[25,47,52], resulting in the slowing down or suppression of the crystal growth (compare Extended Data Fig. 10a (soft system) and Extended Data Fig. 10b (hard system)).

Thus, we can say that a disordered glassy state is more easily destabilized by increasing the ease of preordering, the secondary ordering effectiveness and the degree of the crystal–liquid density matching (Supplementary Figs. 13 and 14). These findings provide crucial information on how we can stabilize a glass state, that is, avoid devitrification, and on what kind of materials we can crystallize even at deep supercooling. Such information should be useful for various industrial applications[53].

Online content

Any methods, additional references, Nature Research reporting summaries, source data, extended data, supplementary information, acknowledgements, peer review information; details of author contributions and competing interests; and statements of data and code availability are available at https://doi.org/10.1038/s41563-021-00993-6.

Received: 23 April 2020; Accepted: 22 March 2021;
Published online: 6 May 2021

References

1. Broughton, J., Gilmer, G. & Jackson, K. Crystallization rates of a Lennard-Jones liquid. *Phys. Rev. Lett.* **49**, 1496–1500 (1982).
2. Jackson, K. A., Gilmer, G. H., Temkin, D. E., Weinberg, J. D. & Beatty, K. Non-equilibrium phase transformations. *J. Cryst. Growth* **128**, 127–138 (1993).
3. Hikima, T., Hanaya, M. & Oguni, M. Microscopic observation of a peculiar crystallization in the glass transition region and β-process as potentially controlling the growth rate in triphenylethylene. *J. Mol. Struct.* **479**, 245–250 (1999).
4. Tanaka, H. Possible resolution of the Kauzmann paradox in supercooled liquids. *Phys. Rev. E* **68**, 011505 (2003).
5. Konishi, T. & Tanaka, H. Possible origin of enhanced crystal growth in a glass. *Phys. Rev. B* **76**, 220201 (2007).
6. Ediger, M., Harrowell, P. & Yu, L. Crystal growth kinetics exhibit a fragility-dependent decoupling from viscosity. *J. Chem. Phys.* **128**, 034709 (2008).
7. Zaccarelli, E. et al. Crystallization of hard-sphere glasses. *Phys. Rev. Lett.* **103**, 135704 (2009).
8. Orava, J. & Greer, A. Fast and slow crystal growth kinetics in glass-forming melts. *J. Chem. Phys.* **140**, 214504 (2014).
9. Gránásy, L. et al. Growth of 'dizzy dendrites' in a random field of foreign particles. *Nat. Mater.* **2**, 92–96 (2003).
10. Gránásy, L., Pusztai, T., Börzsönyi, T., Warren, J. A. & Douglas, J. F. A general mechanism of polycrystalline growth. *Nat. Mater.* **3**, 645–650 (2004).
11. Jackson, K. A. The interface kinetics of crystal growth processes. *Interface Sci.* **10**, 159–169 (2002).
12. Sear, R. P. Nucleation in the presence of slow microscopic dynamics. *J. Chem. Phys.* **128**, 214513 (2008).
13. Tegze, G. et al. Diffusion-controlled anisotropic growth of stable and metastable crystal polymorphs in the phase-field crystal model. *Phys. Rev. Lett.* **103**, 035702 (2009).
14. Wilson, H. W. On the velocity of solidification and viscosity of super-cooled liquids. *Philos. Mag.* **50**, 238–250 (1900).
15. Born, M. & Green, H. S. *A General Kinetic Theory of Liquids* (Cambridge Univ. Press, 1949).
16. Coriell, S. & Turnbull, D. Relative roles of heat transport and interface rearrangement rates in the rapid growth of crystals in undercooled melts. *Acta Metall.* **30**, 2135–2139 (1982).
17. Kawasaki, T. & Tanaka, H. Formation of a crystal nucleus from liquid. *Proc. Natl Acad. Sci. USA* **107**, 14036–14041 (2010).
18. Russo, J. & Tanaka, H. The microscopic pathway to crystallization in supercooled liquids. *Sci. Rep.* **2**, 505 (2012).
19. Tan, P., Xu, N. & Xu, L. Visualizing kinetic pathways of homogeneous nucleation in colloidal crystallization. *Nat. Phys.* **10**, 73–79 (2014).
20. Kratzer, K. & Arnold, A. Two-stage crystallization of charged colloids under low supersaturation conditions. *Soft Matter* **11**, 2174–2182 (2015).

21. Watanabe, K., Kawasaki, T. & Tanaka, H. Structural origin of enhanced slow dynamics near a wall in glass-forming systems. *Nat. Mater.* **10**, 512–520 (2011).
22. Dijkstra, M. & van Roij, R. Entropic wetting in colloidal suspensions. *J. Phys. Condens. Matter* **17**, S3507–S3514 (2005).
23. Page, A. & Sear, R. Freezing in the bulk controlled by prefreezing at a surface. *Phys. Rev. E* **80**, 031605 (2009).
24. Shintani, H. & Tanaka, H. Frustration on the way to crystallization in glass. *Nat. Phys.* **2**, 200–206 (2006).
25. Sun, G., Xu, J. & Harrowell, P. The mechanism of the ultrafast crystal growth of pure metals from their melts. *Nat. Mater.* **17**, 881–886 (2018).
26. Hwang, H., Weitz, D. A. & Spaepen, F. Direct observation of crystallization and melting with colloids. *Proc. Natl Acad. Sci. USA* **116**, 1180–1184 (2019).
27. Tanaka, H., Tong, H., Shi, R. & Russo, J. Revealing key structural features hidden in liquids and glasses. *Nat. Rev. Phys.* **1**, 333–348 (2019).
28. Ashkenazy, Y. & Averback, R. S. Kinetic stages in the crystallization of deeply undercooled body-centered-cubic and face-centered-cubic metals. *Acta Mater.* **58**, 524–530 (2010).
29. Tóth, G. I., Pusztai, T., Tegze, G., Tóth, G. & Gránásy, L. Amorphous nucleation precursor in highly nonequilibrium fluids. *Phys. Rev. Lett.* **107**, 175702 (2011).
30. Tanaka, H. Bond orientational order in liquids: towards a unified description of water-like anomalies, liquid-liquid transition, glass transition, and crystallization. *Eur. Phys. J. E* **35**, 113 (2012).
31. Ashkenazy, Y. & Averback, R. S. Atomic mechanisms controlling crystallization behaviour in metals at deep undercoolings. *Europhys. Lett.* **79**, 26005 (2007).
32. Tegze, G., Tóth, G. I. & Gránásy, L. Faceting and branching in 2D crystal growth. *Phys. Rev. Lett.* **106**, 195502 (2011).
33. Aziz, M. J. Model for solute redistribution during rapid solidification. *J. Appl. Phys.* **53**, 1158–1168 (1982).
34. Dullens, R. P., Aarts, D. G. & Kegel, W. K. Dynamic broadening of the crystal-fluid interface of colloidal hard spheres. *Phys. Rev. Lett.* **97**, 228301 (2006).
35. Gasser, U., Weeks, E. R., Schofield, A., Pusey, P. & Weitz, D. Real-space imaging of nucleation and growth in colloidal crystallization. *Science* **292**, 258–262 (2001).
36. Arai, S. & Tanaka, H. Surface-assisted single-crystal formation of charged colloids. *Nat. Phys.* **13**, 503–509 (2017).
37. Wang, Z., Wang, F., Peng, Y., Zheng, Z. & Han, Y. Imaging the homogeneous nucleation during the melting of superheated colloidal crystals. *Science* **338**, 87–90 (2012).
38. Alsayed, A. M., Islam, M. F., Zhang, J., Collings, P. J. & Yodh, A. G. Premelting at defects within bulk colloidal crystals. *Science* **309**, 1207–1210 (2005).
39. Peng, Y., Wang, Z., Alsayed, A. M., Yodh, A. G. & Han, Y. Melting of colloidal crystal films. *Phys. Rev. Lett.* **104**, 205703 (2010).
40. Li, B. et al. Modes of surface premelting in colloidal crystals composed of attractive particles. *Nature* **531**, 485–488 (2016).
41. Würth, M., Schwarz, J., Culis, F., Leiderer, P. & Palberg, T. Growth kinetics of body centered cubic colloidal crystals. *Phys. Rev. E* **52**, 6415 (1995).
42. Palberg, T. Crystallization kinetics of repulsive colloidal spheres. *J. Phys. Condens. Matter* **11**, R323–R360 (1999).
43. Hynninen, A.-P. & Dijkstra, M. Phase diagrams of hard-core repulsive Yukawa particles. *Phys. Rev. E* **68**, 021407 (2003).
44. Russo, J. & Tanaka, H. Crystal nucleation as the ordering of multiple order parameters. *J. Chem. Phys.* **145**, 211801 (2016).
45. Wang, R., Xu, L.-M. & Wang, F. Molecular-scale processes affecting growth rates of ice at moderate supercooling. *Front Phys. Beijing* **13**, 138116 (2018).
46. Oxtoby, D. W. & Harrowell, P. R. The effect of density change on crystal growth rates from the melt. *J. Chem. Phys.* **96**, 3834–3843 (1992).
47. Ganapathi, D., Chakrabarti, D., Sood, A. & Ganapathy, R. Structure determines where crystallization occurs in a soft colloidal glass. *Nat. Phys.* **17** 114–120 (2020).
48. Podmaniczky, F., Tóth, G. I., Tegze, G. & Gránásy, L. Hydrodynamic theory of freezing: nucleation and polycrystalline growth. *Phys. Rev. E* **95**, 052801 (2017).
49. Delaey, L. *Diffusionless Transformations, Phase Transformations in Materials* (Wiley-VCH, 2001).
50. Tang, S., Wang, J., Svendsen, B. & Raabe, D. Competitive bcc and fcc crystal nucleation from non-equilibrium liquids studied by phase-field crystal simulation. *Acta Mater.* **139**, 196–204 (2017).
51. Tóth, G. I., Tegze, G., Pusztai, T. & Gránásy, L. Heterogeneous crystal nucleation: the effect of lattice mismatch. *Phys. Rev. Lett.* **108**, 025502 (2012).
52. Shibuta, Y. et al. Heterogeneity in homogeneous nucleation from billion-atom molecular dynamics simulation of solidification of pure metal. *Nat. Commun.* **8**, 10 (2017).
53. Zhong, R., Kulovits, A., Wiezorek, J. & Leonard, J. Four-zone solidification microstructure formed by laser melting of copper thin films. *Appl. Surf. Sci.* **256**, 105–111 (2009).

Methods

Experiments. We suspend poly (methyl methacrylate) (PMMA) colloids (diameter $\sigma = 2.2\,\mu m$, polydispersity ~2%, https://www2.ph.ed.ac.uk/~abs/) that were dyed with NBD and grafted with polyhydroxystearic acid, in a mixture of weakly polar and non-polar solvents (iododecane, iododododecane and tetraline; Aldrich) whose refractive index and density are closely matched with those of the colloids. The PMMA particles are negatively charged in our system and interact with each other via a weakly screened Coulomb repulsion, $u(r) = \alpha\exp(-\kappa\sigma(r/\sigma - 1))/(r/\sigma)$ for $r > \sigma$, with $1/\kappa$ being the Debye screening length and α being the effective interaction strength in the suspension. In experiments, the Debye screening length κ^{-1} is obtained through $1/\kappa = (8\pi\lambda_B\rho_{ion})^{-1/2}$. Here $\lambda_B = e^2/4\pi\epsilon_0\epsilon_s k_B T$, where e is the elementary charge, ε_s is the relative dielectric constant of the solvent, and ε_0 is the vacuum permittivity, is the Bjerrum length in the solvent and ρ_{ion} is the number density of ions in the solvent, which is determined by the conductivity of the solvent as $\sigma_s = \rho_{ion}\Lambda/N_A$, with N_A being the Avogadro number and Λ being the molar conductance obtained from Walden's rule[54,55]. We measure the suspension's conductivity and get the solvent conductivity σ_s with the Maxwell–Garnett theory[56].

In our experiments, we adjust κ^{-1} through changing the volume ratio of the weakly polar and the non-polar solvents (from 4:1 to 8:1) and vibrating the solvent with an ultrasonicator, which produces samples with a conductivity ranging from 100 ps cm^{-1} to 1 ns cm^{-1}. The particle volume fraction, ϕ, is below 30%, which leads to the formation of Wigner crystals. The phase diagram is established from the measurements of various samples, as shown in Fig. 1a. The three X symbols indicate the locations of three systems with $\kappa\sigma \approx 2.0$ (bcc stable), $\kappa\sigma \approx 3.2$ (fcc stable) and $\kappa\sigma \approx 5.0$ (fcc stable), where we perform simulations to verify the experimental results.

We first form colloidal crystals inside a rectangular glass capillary (50 mm × 4 mm × 0.2 mm). We use the same solvent used in the colloidal suspension to pretreat the glass capillary, which efficiently prevents particles' adhesion to the smooth wall of the capillary. We then shear-melt the formed crystals and follow the crystallization process by using a Leica SP8 fast confocal microscope (scanning speed, ~10 μm s^{-1} along the z direction). Crystallization starts on the smooth wall, and we measure the kinetics of the wall-assisted crystal growth. We determine each sample's effective temperature in the unit of the melting temperature T_m by comparing the crystal's Lindemann parameter with simulations at the similar $\kappa\sigma$ and ϕ.

Simulations. We use the hard-core repulsive Yukawa (screened Coulomb) potential, $u(r) = \alpha\exp(-\kappa\sigma(r/\sigma - 1))/(r/\sigma)$, to perform simulations. Here, $1/\kappa$ is the Debye screening length, and α is the coefficient of the pair potential. We perform constant temperature (T) simulations for $N = 100{,}000$ particles of mass m in a cuboid box of volume V with mixed boundary conditions (NVT ensemble). We use periodic boundary conditions in the x and y directions, while in the z direction, the boundaries are reflective walls. Here, the reflection means that if a particle moves outside the wall, it will be put back inside the wall while keeping the same distance but changing the sign of the z component of its velocity. The reflective walls reinforce the formation of flat crystalline layers on the walls at the beginning of the phase transition.

The temperature T is controlled by a Nosé–Hoover thermostat[57,58]. The initial configurations are prepared by heating randomly created systems to $1.05T_m$ for 2,000 μs. Then, we quench the homogeneous liquid configurations prepared in this way to the target temperature T. The selected parameters such as mass m, particle diameter σ, volume fraction ϕ and effective Debye screening strength $\kappa\sigma$ in the simulation are the same as in the experiments. The sound speed c in Fig. 1c is obtained by the Newton–Laplace equation: $c = \sqrt{B/\rho}$, where B is the bulk modulus and ρ is the density of the liquid. The chemical potential difference $\Delta\mu(T)$ is obtained by the assumption $\Delta\mu(T) = (T_m - T)\Delta H_m/T_m$, where ΔH_m is the enthalpy of fusion per particle at the melting temperature T_m. The Einstein frequency of the crystal is estimated from $1/\tau_E$, where $\tau_E = \sqrt{k/m}$ and k is the force constant at $T = 0.5T_m$. The k is obtained from the plateau of the mean-square displacement $\langle\Delta r^2\rangle$ using the relation $k = 3k_BT/\langle\Delta r^2\rangle$.

The energy minimization process is performed using the fast inertial relaxation engine method[59]. We quickly quench a high-temperature liquid state ($1.05T_m$) to $T = 0$ and wait until the configuration evolves to the local minimum state. For bulk samples, we use the periodic boundary condition. For samples with a flat wall, we use the same boundary condition as in $T > 0$ simulations.

Bond orientational order and layering order analysis. We capture time-resolved 3D images and perform 3D particle tracking, using IDL[60] to extract all particles' positions as a function of time. In this work, we use the bond orientational order parameters, q_l and w_l, and their coarse-graining versions, $\bar{q}_l$ and $\bar{w}_l$, to quantify the single-particle-level local structures[18,19,36,61–63].

We first calculate the local bond orientational function $q_{lm}(i) = \sum_{f\in F(i)} \frac{A(f)}{A} Y_{lm}(\theta_{ij}, \phi_{ij})$, where $A(f)$ is the surface area of the Voronoi cell facet f separating centre particle i and its neighbour j; A is the total surface area of the Voronoi cell boundary $F(i)$; $Y_{lm}(\theta_{ij}, \phi_{ij})$ are the spherical harmonics with $m \in [-l, l]$; and θ_{ij} and ϕ_{ij} are the polar and azimuthal angles of the vector $\mathbf{r}_{ij} = \mathbf{r}_i - \mathbf{r}_j$, where $\mathbf{r}_i$ is the position vector of particle i and $\mathbf{r}_j$ is the position vector of its neighbouring particle j.

The coarse-graining version is calculated as $Q_{lm} = \frac{1}{N_b}\sum_{k=0}^{N_b} q_{lm}(k)$, with N_b being the number of neighbours determined by Voronoi cell analysis. Then, we obtain the rotationally invariant coarse-grained order parameters of particle i, $\bar{q}_l(i)$ and $\bar{w}_l(i)$, as follows: $\bar{q}_l(i) = \left(\frac{4\pi}{2l+1}\sum_{m=-l}^{l}|Q_{lm}(i)|^2\right)^{1/2}$ and $\bar{w}_l(i) = \sum_{m_1+m_2+m_3=0}^{l} \begin{pmatrix} l & l & l \\ m_1 & m_2 & m_3 \end{pmatrix} \frac{Q_{lm_1}(i)Q_{lm_2}(i)Q_{lm_3}(i)}{(\sum_{m=-l}^{l}|Q_{lm}(i)|^2)^{3/2}}$.

At each temperature T, we first calculate the $\bar{q}_6$ value of the final equilibrium crystal $\bar{q}_6^F(T)$ and the initial liquid state $\bar{q}_6^I(T)$. Then we define a threshold value $\bar{q}_6^*$ corresponding to 75% position of their relative value: $\bar{q}_6^*(T) = 0.75\bar{q}_6^F(T) + 0.25\bar{q}_6^I(T)$. At each temperature T, we identify particles with $\bar{q}_6 < \bar{q}_6^*$ as liquid structures and particles with $\bar{q}_6 \geq \bar{q}_6^*$ as the initial solid structures. This definition reduces the ambiguity of the $\bar{q}_6$ change caused by thermal distortions when we need to identify solid structures across a huge temperature range ($0–0.9T_m$). In the solid structures, we identify bcc solid particles with $\bar{w}_6 \geq 0$ and rhcp solid particles (a mixture of fcc and hexagonal close-packed (hcp)) with $\bar{w}_6 < 0$. The rhcp solids are then divided into fcc and hcp by using the segregation in the q_4–w_4 distribution map.

We introduce the Lindemann parameter δL. Here, $\delta L = \delta/a$, where δ^2 is the height of the time-independent plateau of the mean-square displacement $\langle\Delta\mathbf{r}^2(t)\rangle$ and a is the lattice constant.

To quantify the layering order of particle i, we introduce a single-particle-level layering order parameter $L_a(i)$. We first find the particle set within a volume around particle i: $Ne(i) = \{(x, y, z) \in U | |x - x_i| < \Delta, |y - y_i| < \Delta, |z - z_i| < d\}$, where Δ is set to 1.2 times of the lattice constant a, and d is 1.2 times the distance between neighbouring layers perpendicular to the wall (that is, the z direction). Then, we partition all the elements into three subsets, S_{-1}, S_0 and S_1 (the upper, middle and lower layers, respectively) to minimize $\Sigma_{j=-1}^{1}|z - \bar{z}_j|^2$, where $z_j = \{z|(x, y, z) \in S_j\}$. Then, the parameter L_a of particle i is defined as $L_a(i) = \frac{\mathrm{var}(S_{-1}) + \mathrm{var}(S_0) + \mathrm{var}(S_1)}{3d}$, where var(·) represents the variance of z_j.

We can regard $L_a(i)$ as a 1D version of the Lindemann parameter, which quantifies the positional fluctuation deviated from the lattice sites. This parameter allows us to distinguish unlayered and crystalline particles. For example, unlayered liquid particles have $L_a \approx 0.22$, whereas crystalline particles usually have $L_a < 0.14$, as shown in Extended Data Fig. 1a ($\kappa\sigma \approx 2.0$, $T \approx 0.6T_m$). Note that perfect lattices with no thermal fluctuations have $L_a = 0$.

The icosahedron-like structure is identified using the analysis of Voronoi tessellation. We first identify regular tetrahedrons formed by particle i and its neighbours using the criterion that the standard deviation of each tetrahedron's edge length is ≤0.1. Then, we identify the five-membered pentagonal ring structure connected by five face–face connected regular tetrahedrons, which is the elementary structural unit of a full icosahedron (a perfect icosahedron has twelve rings). Particles with three or more pentagonal rings are identified as icosahedron-like particles. Nearly perfect icosahedron structure can be identified in terms of the number of pentagonal rings.

The layering of liquid particles. When two neighbouring particles have very similar local environments, they are said to be connected with one solid bond. The solid bond number for any particle i is defined as $\xi(i) = \Sigma_{j=1}^{N_b(i)}(H(d_l(i, j) - d_c)$, with H being the Heaviside step function, $d_c = 0.7$ being the threshold value and $d_l(i, j) = \frac{\Sigma_{m=-l}^{l} q_{lm}(i)q_{lm}^*(j)}{(\Sigma_{m=-l}^{l}|q_{lm}(i)|^2)^{1/2}(\Sigma_{m=-l}^{l}|q_{lm}(j)|^2)^{1/2}}$ quantifying the similarity of the local environment between particle i and particle j. For the layered particles at the interface ($L_a < 0.14$ and $\bar{q}_6 < \bar{q}_6^*$), we can further classify them into the 'solid surface', which should be intrinsically layered, and the true 'interface liquid', which is induced to be layered. We identify layered particles at the interface that have $\xi(i) \geq 5$ as the solid surface, and the ones having $\xi_c < 5$ as the layered 'interface liquid'. The relevance of this classification is supported by the probability distribution of the solid bond number $\xi(i)$ and $L_a(i)$ in Extended Data Figs. 1b and 1c, respectively.

As shown in the counting plots on the $L_a - \bar{q}_6$ plane (Extended Data Fig. 2a–f), the $\bar{q}_6$ starts to increase with an increase in the degree of layering, more precisely, when L_a becomes smaller than ~0.14 for both experiments and simulations. We can see a bridging region connecting the unlayered-particle and crystalline-particle islands, which we call the 'layered bridge' and which contains both the solid surface and interface liquid. We also show the temporal evolution of these order parameters in Extended Data Fig. 2g, which tells us the kinetic pathway of crystallization. We can see that the layered- liquid region spread out from the unlayered (bulk)-liquid region (the lower-right islands in each panel) towards the crystalline-particle region (the upper-left island in each panel). In the early stage, the flat wall induces the layered liquid with crystalline orientational order. Then, this layered liquid transforms into the crystal. Thus, we may say that the layered liquid is an intermediate preordered state of crystallization.

The definition of crystal growth speed. For all samples of various $\kappa\sigma$ and T in contact with a flat wall, crystallization first starts from the flat wall. The solid fractions grow linearly with the time t until spinodal nucleation (the nucleation barrier in bulk samples becomes comparable with k_BT, $T_{sp} \approx 0.7T_m$) eventually

happens inside the bulk for low-T samples, as shown in Extended Data Fig. 3a (see the inset figure for the nucleus generated in the bulk liquid region). We then define the crystal growth speed v before spinodal nucleation happens, using a linear fit: $v = N_{solid}(t)d/N_0$, where $N_{solid}(t)$ is the solid particle number at time t, d is the layer–layer distance and N_0 is the average particle number per layer. By comparison, the crystallization for bulk samples is illustrated in Extended Data Fig. 3b, which is much slower than the speed of wall-assisted crystallization (the dashed line).

The crystal growth mode with the rough and thick interface. At each temperature T, we define the interface roughness h as the distance over which the parameter $\bar{q}_6(z)$ changes from 10% ($0.1\bar{q}_6^{F}(T) + 0.9\bar{q}_6^{I}(T)$) to 75% ($0.75\bar{q}_6^{F}(T) + 0.25\bar{q}_6^{I}(T)$, which equals $\bar{q}_6^{\star}$) of its value in the final crystal relative to its value in the unlayered fluid[32,34]. We define the thickness l of the interface as the total particle number of preordered particles ($L_a < 0.14$ and $\bar{q}_6 < \bar{q}_6^{\star}$) divided by the average particle number N_0 per layer. We can see the similar rough and thick feature of the interface at all T values as shown by the quantities h (top), l (middle) and l/h (bottom) in Extended Data Fig. 4a. The solid–surface thickness ($l_s = N_{\tilde{s}(i)\geq 5}/N_0$) is comparable with the interface-liquid thickness ($l - l_s$) at all T, as shown by the quantities l_s (top), $l - l_s$ (middle) and $l_s/(l - l_s)$ (bottom) in Extended Data Fig. 4b. This rough, thick and layered nature of the interface is not affected by the increasing amounts of icosahedron-like structures in the bulk due to deeper supercooling, as shown by the comparison of $f_{layered}$ (fraction of layered particle at interface; top), $f_{unlayered}$ (fraction of unlayered particle at interface; middle) and f_{ico} (fraction of icosahedron-like particle in bulk layers; bottom) in Extended Data Fig. 4c.

We observe an island-growth mode consisting of vertical ($\perp$) and lateral ($\parallel$) growth in Fig. 1h,i. To calculate $v_\perp(x,y)$, we first select two particle layers at the interface, and then define a $3a \times 3a$ area for particle i in the x–y plane, $x_i - 1.5a < x < x_i + 1.5a$, $y_i - 1.5a < x < y_i + 1.5a$. After Δt, we search for the increasing amount of solid particles $N_\perp$ in the z direction and the increasing amount of solid particles $N_\parallel$ within the two particle layers. We define $v_\perp = \frac{N_\perp Sd}{N_0(3a)^2}$ and $v_\parallel = \frac{N_\parallel Sd}{N_0(3a)^2}$, where N_0/S is the average area per particle in the x–y plane.

We can see in Extended Data Fig. 5a–c the crystal growth kinetics at various T under the competition between the rough, thick interface and the geometric frustration due to icosahedron-like structures. Corresponding to the rough, thick and layered feature of the interface shown by the contour plot of $h(x,y)$ and $L_a(x,y)$ (see the first and second rows of Extended Data Fig. 5a–c, respectively), we robustly observe an island-growth mode consisting of vertical and lateral growth, as shown in the third and fourth rows, respectively, of Extended Data Fig. 5a–c. At low T ($T \leq 0.5T_m$), the large amounts of icosahedron-like structures are eliminated mainly by the lateral growth (Extended Data Fig. 5a; experiment), whereas icosahedron-like structures are less frequent in higher-T samples (Extended Data Fig. 5b) and have little effect on the growth mode near T_m (Extended Data Fig. 5c).

The island-growth mode at low T is a collective process determined by the interface's thickness. We can see in Extended Data Fig. 6 that during the ordering time Δt typical of one particle layer, the propagation length of the interface is approximately equal to the thickness l, which suggest that the crystal growth speed can be estimated by $v \approx l/\Delta t$.

The definition of the layering and further ordering. Based on the structural-ordering pathways shown in Extended Data Fig. 7, we can divide the ordering kinetics into two repetitive steps: the rapid increase of $\bar{q}_6$ (from the left side of the unlayered-liquid part, $L_a \approx 0.14$, to the solid–liquid boundary, $\bar{q}_6 \approx \bar{q}_6^{\star}$), which corresponds to the layering process, and the further slow growth of $\bar{q}_6$ inside the solid phase (from $\bar{q}_6 \approx \bar{q}_6^{\star}$ to $\bar{q}_6 \approx \bar{q}_6^{F}$), which corresponds to the repairing of the quenched-in disorder. We universally find the similar periodic two-step ordering in both simulations and experiments, as shown in Extended Data Fig. 7b–f.

Thus, we define the time spent for a liquid particle to join the crystal phase as the time duration for crossing the layered liquid state, which starts from the moment of the first and fast increase of $\bar{q}_6$ around $L_a \approx 0.14$ until the moment when $\bar{q}_6$ reaches $\bar{q}_6^{\star}$. For each particle i, thus, we define the starting point of the layering period as the time when $L_a(i)$ approaches ~0.14 and its ending point as the time when $\bar{q}_6$ first exceeds $\bar{q}_6^{\star}$. The moving distance is then defined as the particle displacement during this period.

Orientation-sensitive bond orientational order parameters. Structural transformations in solids generally require a specific orientational relationship between the parent and the product structures. Because the bond orientational order parameters, $\bar{q}_l$ and $\bar{w}_l$, are rotationally invariant, they cannot be used for detecting the possible specific orientational connections. By using the spherical projection method, which keeps the orientational information, we examine the local-order development for a group of interface particles ($L_a < 0.14$) that grow to the same crystalline grain. We classify them into three parts based on their $\bar{q}_6(i)$: interface stage ($\bar{q}_6(i) < \bar{q}_6^{\star}$), initial solid ($\bar{q}_6^{\star} < \bar{q}_6(i) < 0.4$) and final solid ($\bar{q}_6(i) > 0.4$). For each particle in the three groups, we first set its position as a central reference point ($x = y = z = 0$) and then plot the relative positions of all its neighbouring particles (within the first minimum distance of the radial distribution function $g(r)$). Then, we take its average both in time and space. Such a transformation keeps the orientational information of this group of particles and thus, enables us to examine the orientation connections between the preordered interface and product crystal during the structural ordering.

Data availability

Source data are provided with this paper. All other data that support the plots within this paper and other findings of this study are available from the corresponding authors upon reasonable request.

Code availability

The computer codes used in this paper are available from the corresponding authors upon reasonable request.

References

54. Walden, P. Organic solvents and ionization media. III. Interior friction and its relation to conductivity. *Z. Phys. Chem.* **55**, 207–249 (1906).
55. Royall, C., Leunissen, M. & van Blaaderen, A. A new colloidal model system to study long-range interactions quantitatively in real space. *J. Phys. Condens. Matter* **15**, S3581–S3596 (2003).
56. Maxwell-Garnett, J. C. Colours in metal glasses and in metallic films. *Philos. Trans. R. Soc. A* **203**, 385–420 (1904).
57. Plimpton, S. *Fast Parallel Algorithms for Short-Range Molecular Dynamics* (Sandia National Labs, 1993).
58. Nosé, S. A unified formulation of the constant temperature molecular dynamics methods. *J. Chem. Phys.* **81**, 511–519 (1984).
59. Bitzek, E., Koskinen, P., Gähler, F., Moseler, M. & Gumbsch, P. Structural relaxation made simple. *Phys. Rev. Lett.* **97**, 170201 (2006).
60. Crocker, J. C. & Grier, D. G. Methods of digital video microscopy for colloidal studies. *J. Colloid Interface Sci.* **179**, 298–310 (1996).
61. Steinhardt, P. J., Nelson, D. R. & Ronchetti, M. Bond-orientational order in liquids and glasses. *Phys. Rev. B* **28**, 784 (1983).
62. Lechner, W. & Dellago, C. Accurate determination of crystal structures based on averaged local bond order parameters. *J. Chem. Phys.* **129**, 114707 (2008).
63. Mickel, W., Kapfer, S. C., Schröder-Turk, G. E. & Mecke, K. Shortcomings of the bond orientational order parameters for the analysis of disordered particulate matter. *J. Chem. Phys.* **138**, 044501 (2013).

Acknowledgements

This work is supported by National Natural Science Foundation of China grant no. 11774059, no. 11734014, no. 11935002, no. 11525520, no. 11725521 and no. 12035004; Science and Technology Commission of Shanghai Municipality under grant no. 20JC1414700 and Shanghai Rising Star programme grant no. 16QA1400600; National Key Research and Development Program of China (grant no. 2016YFA0300901); and Hong Kong RGC (GRF 14306518 and GRF 14303415). H. Tanaka acknowledges Grants-in-Aid for Scientific Research (A) (JP18H03675) and Specially Promoted Research (JP25000002 and JP20H05619) from the Japan Society of the Promotion of Science.

Author contributions

P.T., H. Tanaka and Limei Xu supervised the project. P.T., Q.G. and S.T. performed the experiments, J.A. and H. Tong performed the numerical simulations. All authors contributed to the data analysis. P.T. and H. Tanaka wrote the manuscript.

Competing interests

The authors declare no competing interests.

Additional information

Extended data is available for this paper at https://doi.org/10.1038/s41563-021-00993-6.

Supplementary information The online version contains supplementary material available at https://doi.org/10.1038/s41563-021-00993-6.

Correspondence and requests for materials should be addressed to Limei Xu, H. Tanaka or P.T.

Reprints and permissions information is available at www.nature.com/reprints.

Peer review Information *Nature Materials* thanks László Gránásy and Thomas Palberg for their contribution to the peer review of this work.

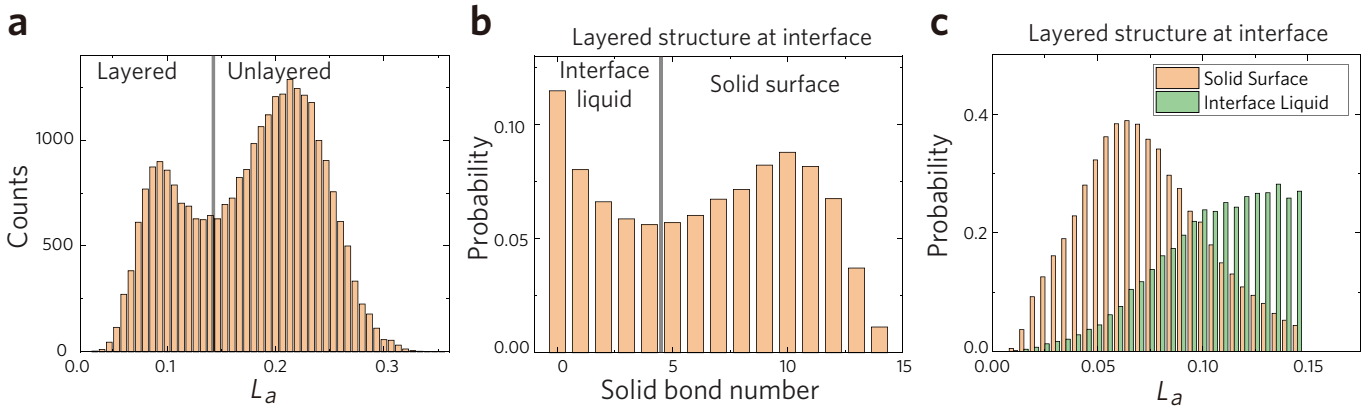

Extended Data Fig. 1 | Layering property of interface particles. a, Histogram of $L_a(i)$ for all particles at the initial crystal growth stage. It can efficiently distinguish layered particles from unlayered particles. **b**, Histogram of $\xi(i)$ for the layered particles in **a**. The layered particles at interface contains both the solid surface and interface liquid. **c**, Histogram of $L_a(i)$ for solid surface particles and interface liquid particles respectively.

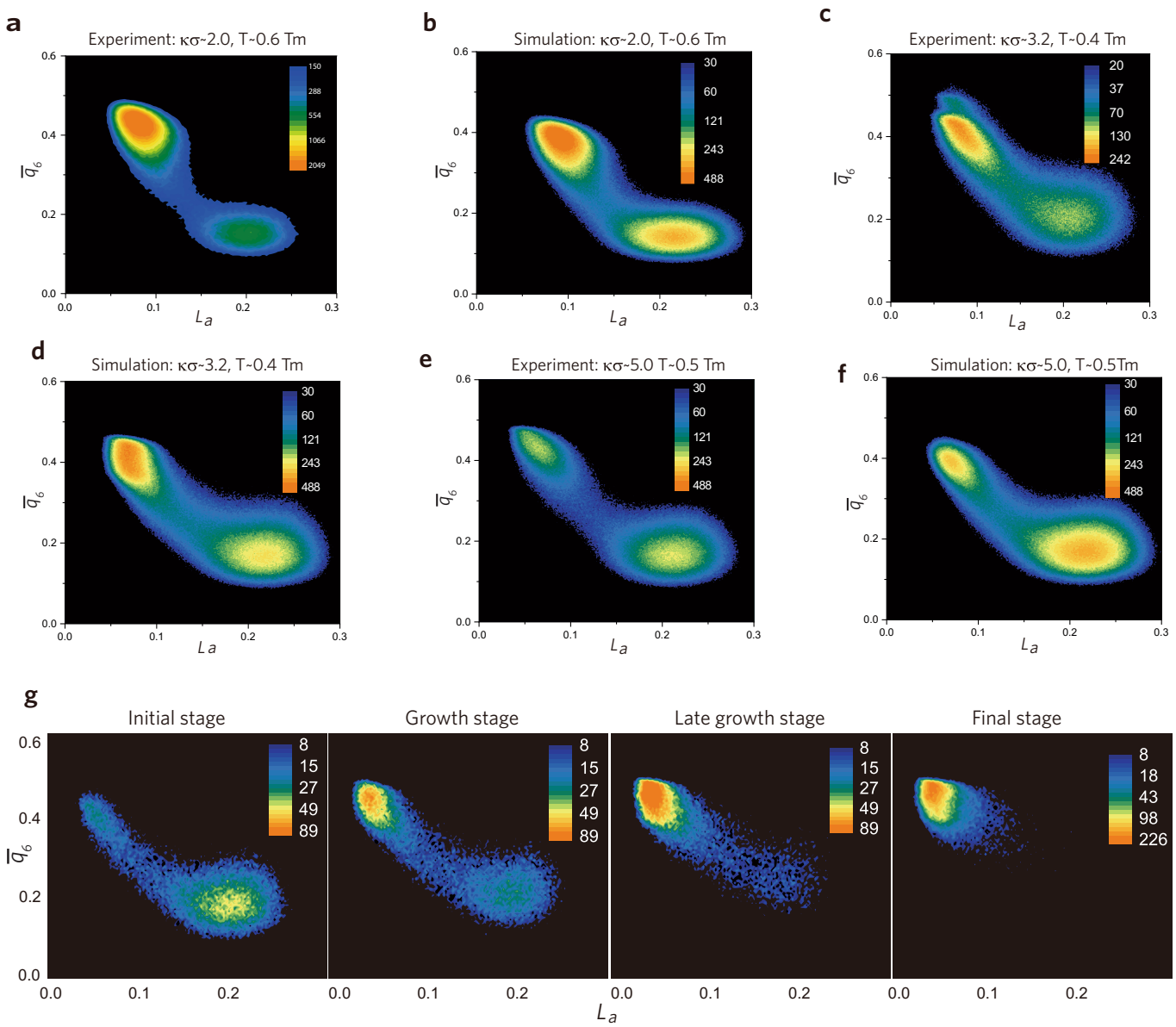

Extended Data Fig. 2 | Particle counts in the $L_a - \bar{q}_6$ parameter space for experiments and simulations. **a**,$\kappa\sigma \sim 2.0$, $T \sim 0.6T_m$ in experiments. **b**,$\kappa\sigma \sim 2.0$, $T \sim 0.6T_m$ in simulations. **c**,$\kappa\sigma \sim 3.2$, $T \sim 0.4T_m$ in experiments. **d**,$\kappa\sigma \sim 3.2$, $T \sim 0.4T_m$ in simulations. **e**,$\kappa\sigma \sim 5.0$, $T \sim 0.5T_m$ in experiments. **f**,$\kappa\sigma \sim 5.0$, $T \sim 0.5T_m$ in simulations. We can identify the layering of liquid as the region spreading out from the solid part (the upper-left island in each panel) towards the unlayered liquid (the lower-right island in each panel). **g**, Time evolution of the particle counts in the $L_a - \bar{q}_6$ parameter space. From left to right: the initial, early-growth, late-growth, and final stages.

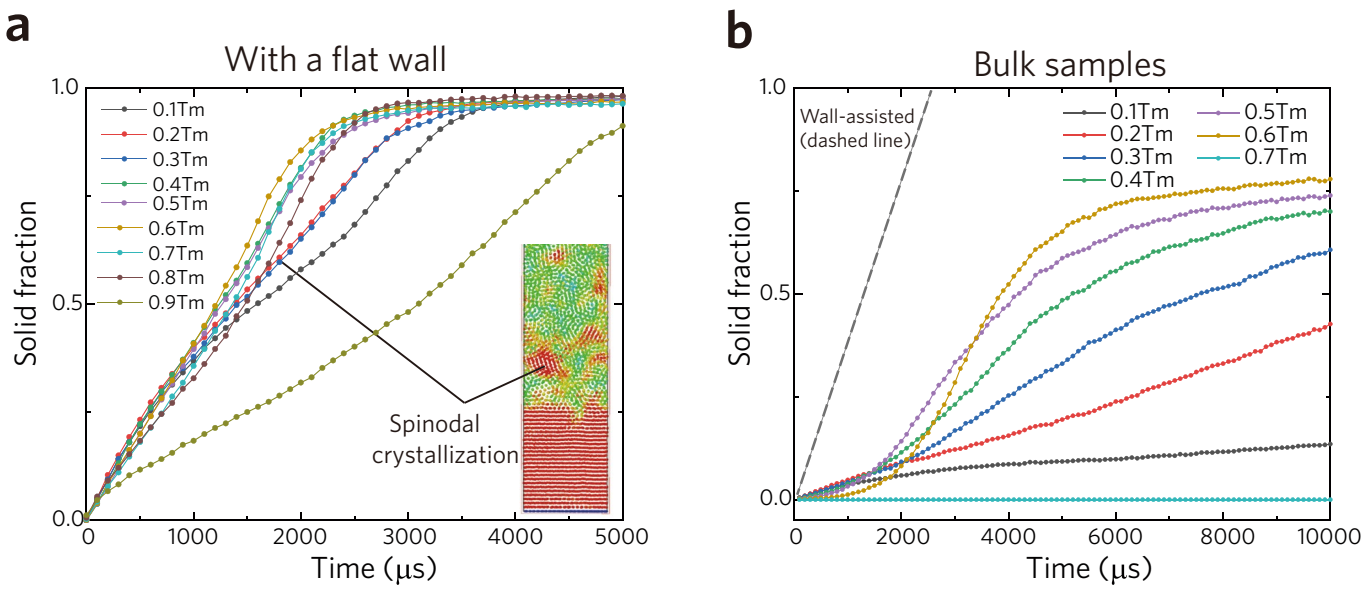

Extended Data Fig. 3 | Comparison of the crystallization process with a flat wall and in bulk in simulations at various T ($\kappa\sigma \sim 2.0$). a, The solid fraction versus the time t for samples with a flat wall. We observe a fast wall-assisted crystallization until the growth front meets the small crystal nucleus caused by spinodal nucleation inside the sample (see inset figure). **b**, The solid fraction versus the time t for bulk samples. The crystallization speed is much lower than in **a**, which is approximately indicated by the dashed line.

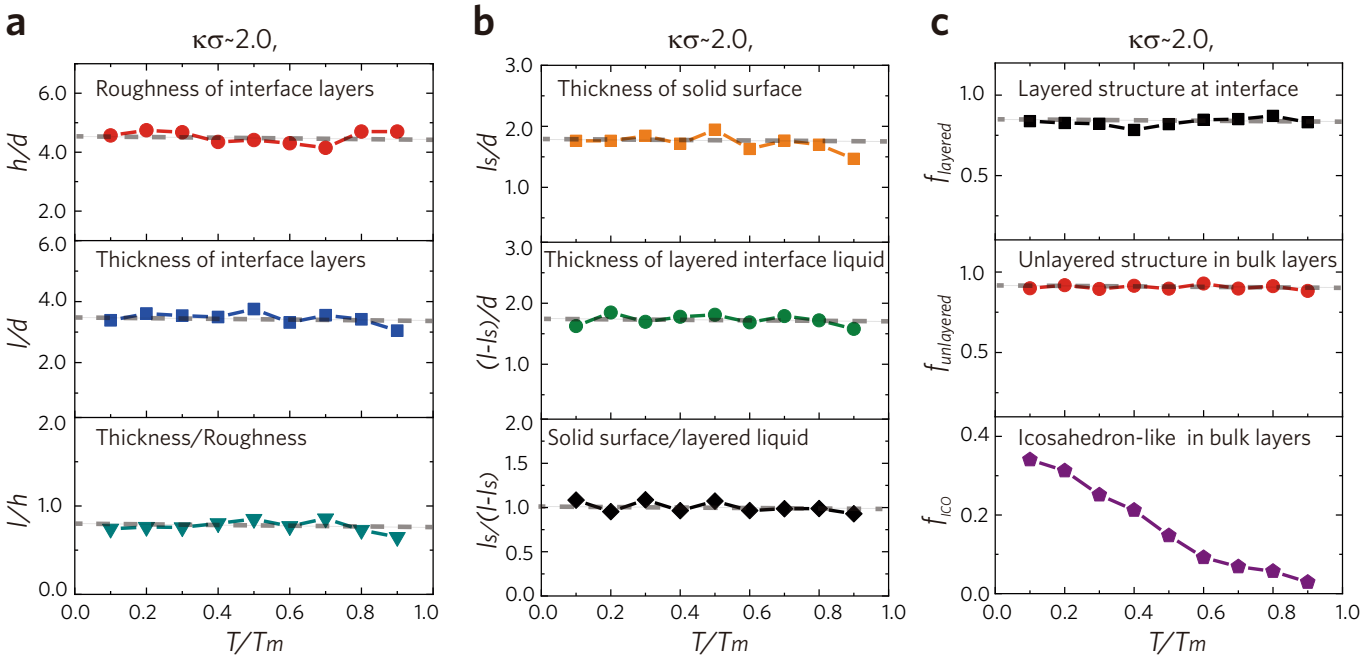

Extended Data Fig. 4 | The rough and thick interface profile at various T ($\kappa\sigma \sim 2.0$). a, The T-dependence of the roughness h, thickness l and l/h. The interface is rough and thick at all T ($h \sim 4.6d$, $l \sim 3.5d$), At each panel, the grey line indicates the average value. **b**, The T-dependence of the solid surface thickness l_s, interface liquid thickness $l - l_s$ and $l_s/(l - l_s)$. **c**, The T-dependence of $f_{layered}$ (fraction of layered particle at interface), $f_{unlayered}$ (fraction of unlayered particle at interface) and f_{ico} (fraction of icosahedron-like particle in bulk layers). This rough, thick and layered nature of the interface is little affected by the increasing amounts of icosahedron-like structures in the bulk due to deeper supercooling.

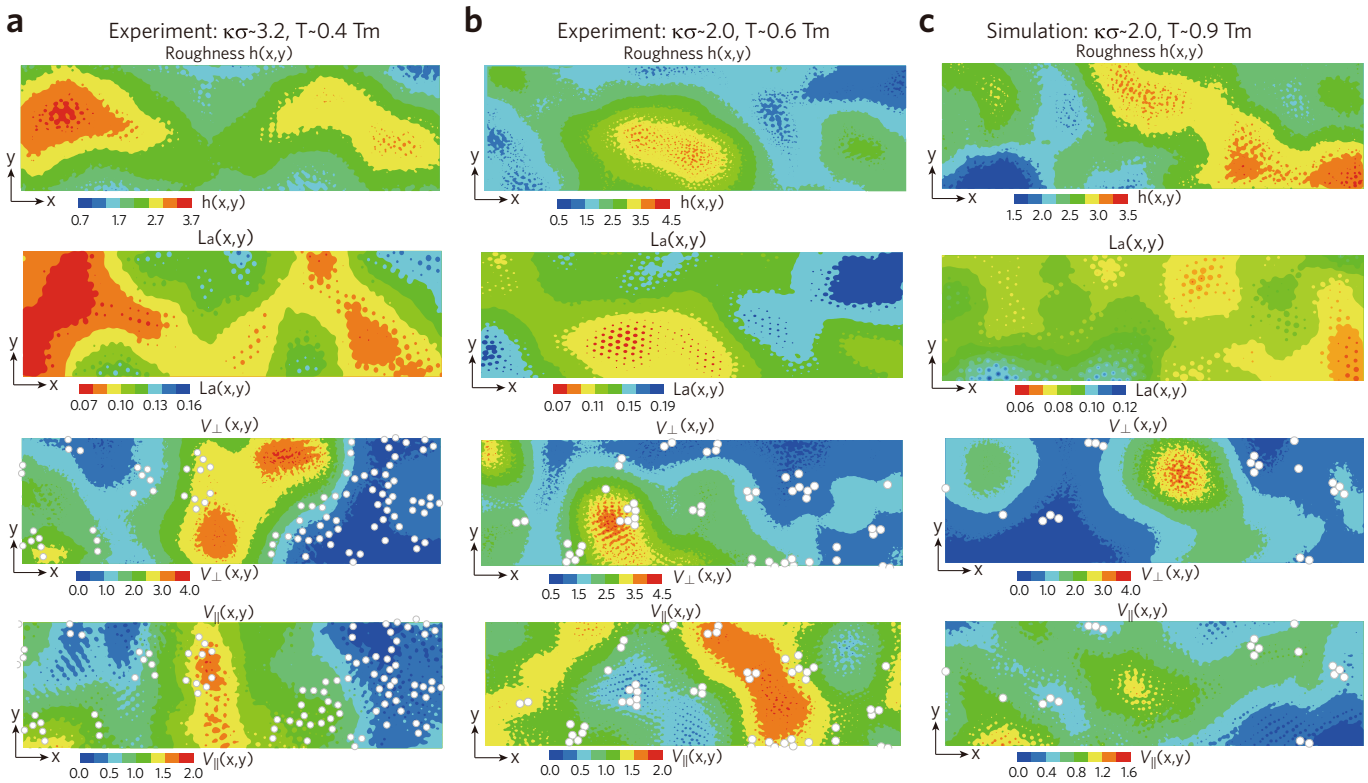

Extended Data Fig. 5 | The island-growth mode of crystal for rough and thick interface at other $\kappa\sigma$ and T in experiments and simulations. a, Contour plot of the height of the crystal front $h(x,y)$, $L_a(x,y)$, $v_{ver}(x,y)$ and $v_{lat}(x,y)$ (from top to bottom respectively, $\kappa\sigma \sim 3.2$, $T \sim 0.4T_m$ in experiments. **b, c** The same quantities as in **a** for $\kappa\sigma \sim 2.0$, $T \sim 0.6T_m$ in experiments (**b**) and $\kappa\sigma \sim 2.0$, $T \sim 0.9T_m$ in simulations (**c**). At all $\kappa\sigma$ and T, we observe the vertical growth mode generating new islands and lateral growth mode around the island. The icosahedron-like particles at the interface (white spheres) is mainly eliminated by the lateral growth in **a**. Icosahedron-like structures are less frequent in higher-T samples and thus have little effect on the growth mode in **c**.

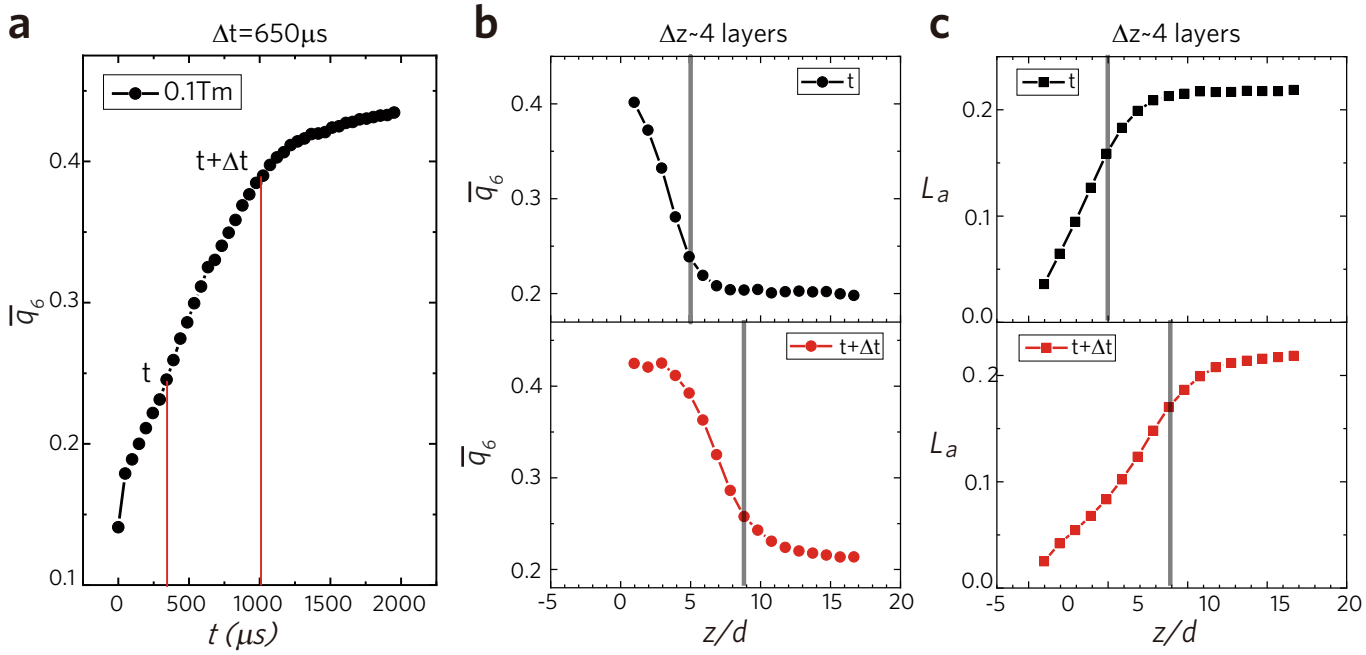

Extended Data Fig. 6 | The collective ordering process determined by the interface thickness. a, The evolution of $\bar{q}_6$ for one particle layer with respect to time t ($\kappa\sigma \sim 2.0$, $T \sim 0.1T_m$ in simulations). The time period Δt (in between red lines) corresponds to a propagation length $4d$ of the growth front. **b**, The interface profile $\bar{q}_6(z)$ with respect to z/d at t (top) and $t+\Delta t$ (bottom). The propagation length during Δt is illustrated by the distance between the two grey lines. **c**, The interface profile $L_a(z)$ with respect to z/d at t (top) and $t+\Delta t$ (bottom). It supports a collective crystal growth process with the crystal growth speed expressed as: $v = l/\Delta t$.

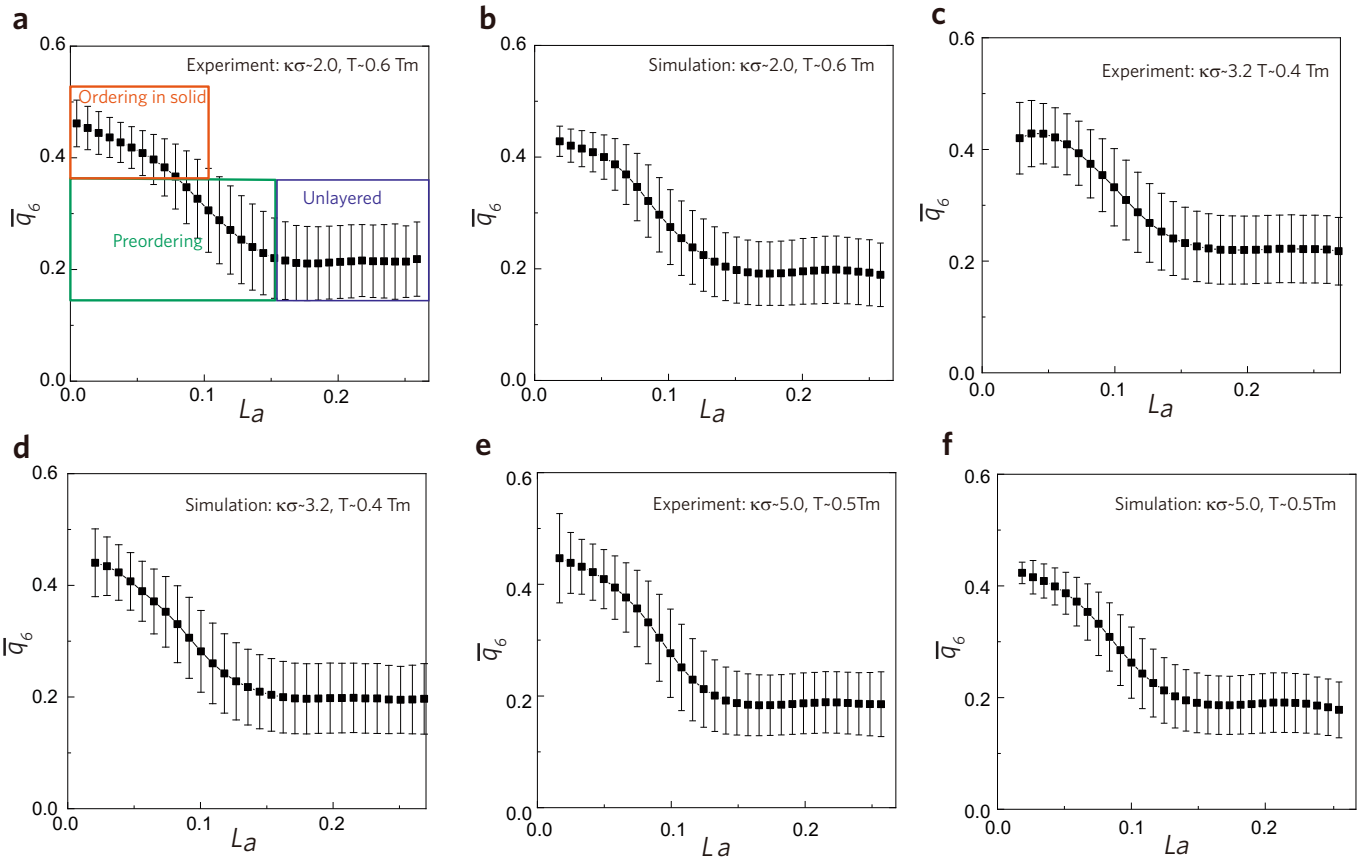

Extended Data Fig. 7 | Definition of the preordering and the further ordering based on the $L_a - \bar{q}_6$ correlation. a, b, The $L_a - \bar{q}_6$ correlation at $\kappa\sigma \sim 2.0$, $T \sim 0.6T_m$ in experiments (**a**) and simulations (**b**). **c, d**, The $L_a - \bar{q}_6$ correlation at $\kappa\sigma \sim 3.2$, $T \sim 0.4T_m$ in experiments (**c**) and simulations (**d**). **e,f**, The $L_a - \bar{q}_6$ correlation at $\kappa\sigma \sim 5.0$, $T \sim 0.5T_m$ in experiments (**e**) and simulations (**f**). The fast increase of $\bar{q}_6$ (from the left side of the unlayered liquid part, $L_a \sim 0.14$, to the solid-liquid boundary, $\bar{q}_6 \sim \bar{q}_6^{\star}$) corresponds to the preordering process, whereas the further slow growth of $\bar{q}_6$ inside the solid phase (from $\bar{q}_6 \sim \bar{q}_6^{\star}$ to $\bar{q}_6 \sim \bar{q}_6^{f}$) corresponds to the repairing of the 'quenched-in disorder'. The error bars represent the standard deviation of the $\bar{q}_6$ values corresponding to the values of L_a within a small binsize (the symbol-symbol distance on *x* axis).

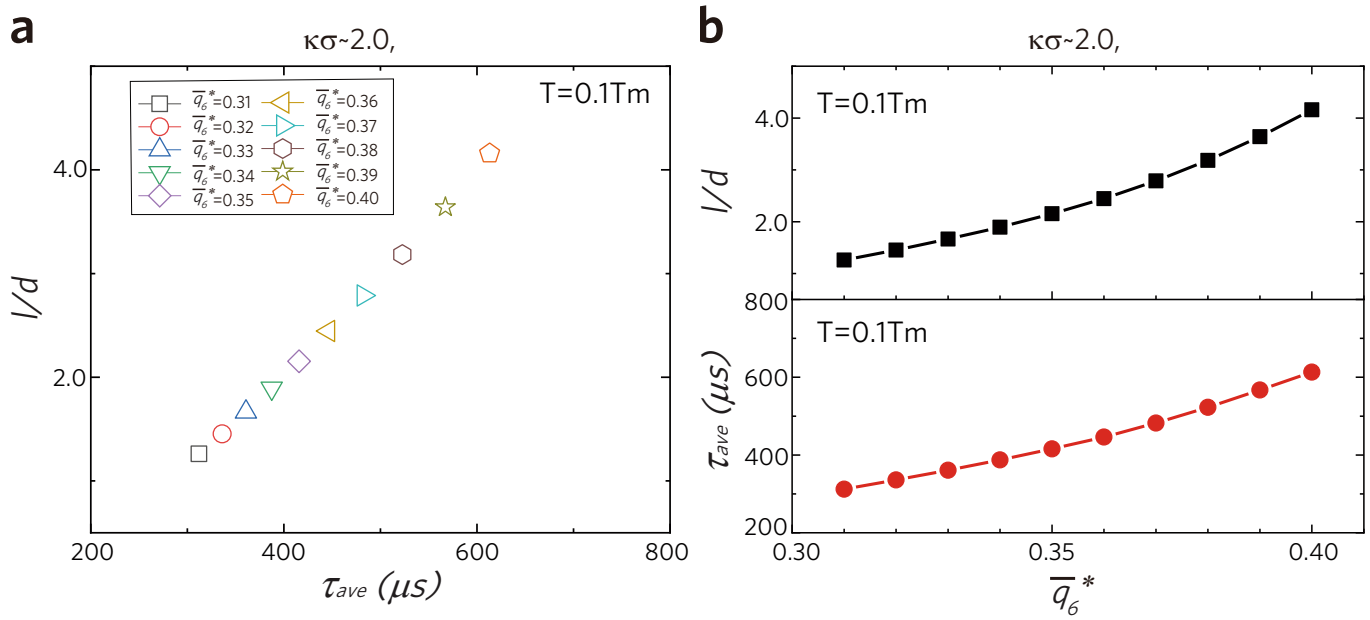

Extended Data Fig. 8 | The correlation of *l* and τ_{ave} with the choice of $\overline{q}_6^\star$. **a**,*l* versus τ_{ave} with different choice of $\overline{q}_6^\star$. **b**, the $\overline{q}_6^\star$-dependence of *l* (top) and τ_{ave} (bottom). Although the selection of the threshold value of $\overline{q}_6^\star$ weakly modifies the values of *l* and τ_{ave}, it affects them proportionally, and thus produces little change in l/τ_{ave}. Such proportionality between the length scale of collective motion and its time scale is a genuine feature of diffusionless collective rearrangements.

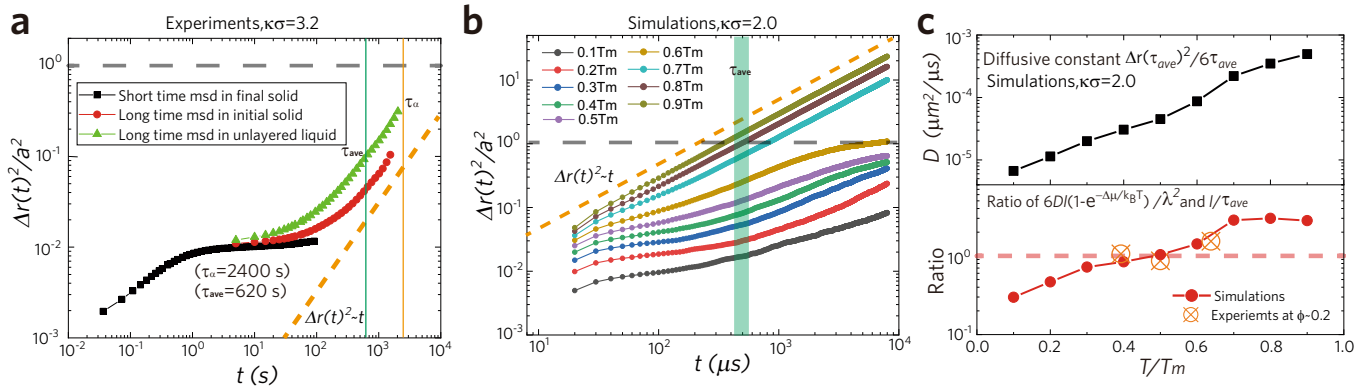

Extended Data Fig. 9 | Diffusive motion and the comparison with diffusionless ordering model. a, The time evolution of the mean-square displacement $\Delta r(t)^2$ for final crystals, initial crystals, and unlayered liquid in experiments ($\kappa\sigma \sim 3.2$, $T \sim 0.4T_m$). We illustrate τ_{ave} and τ_α by vertical green and orange lines, respectively. **b**, The time evolution of the mean-square displacement $\Delta r(t)^2$ for bulk samples at various T in simulations ($\kappa\sigma \sim 2.0$). we illustrate τ_{ave} by vertical green line. The subdiffusive behavior becomes obvious at deep supercoolings. **c**, The diffusive constant determined in **b** and the comparison between diffusive and diffusionless models. Diffusive constant D (top) is determined as $\Delta r(\tau_{ave})^2/6\tau_{ave}$.

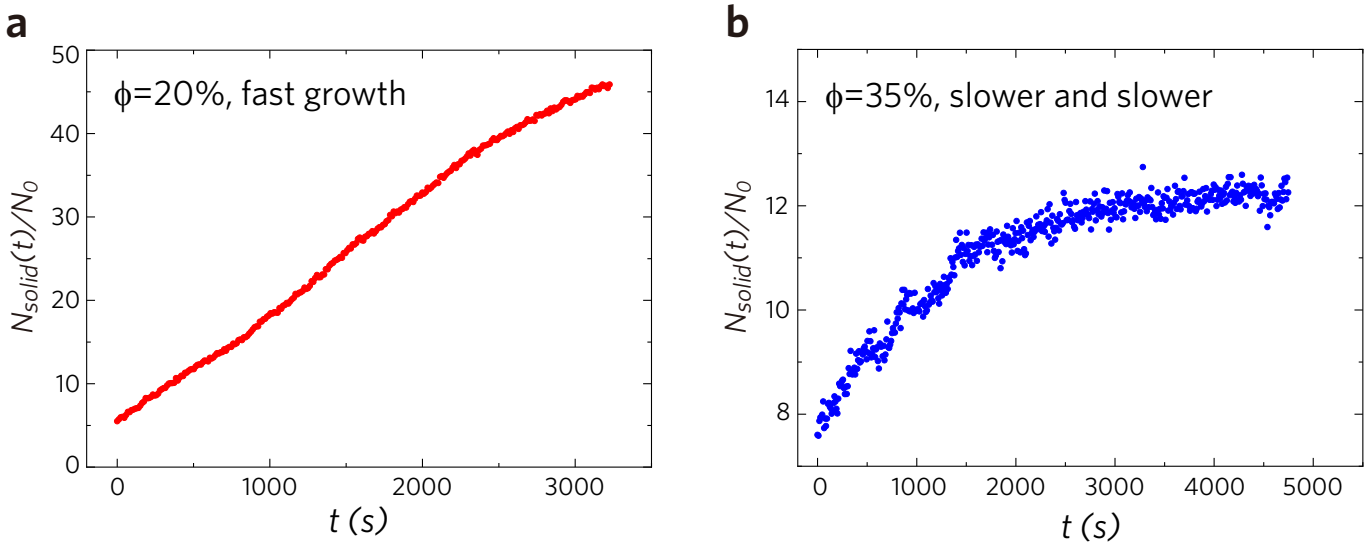

Extended Data Fig. 10 | The comparison of low-ϕ and high-ϕ crystal growth at deep supercooling in experiments. a, The continuous fast crystal growth at $\phi = 20$ %, where the interaction is soft-repulsive. The fast crystal growth modes can propagate more than 40 particle layers. **b**, Crystal growth for $\phi = 35$ % sample, where the hard-core effect is prominent. Crystal growth becomes slower and slower as the accumulation of trapped-in defects. There is no homogeneous nucleation behavior observed inside the sample.